(3)

Measurement of Glucose in Human Blood Serum Using Near-Infrared Raman Spectroscopy

by

Tae-Woong Koo

B.S., Mechanical Engineering (1996)
Seoul National University

Submitted to the Department of Mechanical Engineering
in Partial Fulfillment of the Requirements for the Degree of Master of Science in Mechanical Engineering

at the

Massachusetts Institute of Technology

February 1998

Author .....
Department of Mechanical Engineering
January 22, 1998

Certified by .....
Michael S. Feld
Professor of Physics
Thesis Supervisor

Read by .....
Derek Rowell
Professor of Mechanical Engineering
Thesis Reader

Accepted by .....
Ain A. Sonin
Chairman, Departmental Committee on Graduate Students

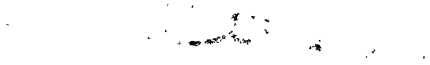

Measurement of Glucose in Human Blood Serum Using Near-Infrared Raman Spectroscopy

by

Tae-Woong Koo

Submitted to the Department of Mechanical Engineering
on January 22, 1998 in partial fulfillment of the
requirements for the Degree of
Master of Science in Mechanical Engineering

Abstract

This thesis discusses the development of a near infrared spontaneous Raman scattering spectroscopic system designed to analyze blood chemical composition in human blood serum. Several analytic methods have been studied and verified for analyzing the Raman spectrum. Three experiments have been performed with a step by step approach to isolate and solve problems.

Using this Raman spectroscopic system, we measured the glucose concentration level in phosphate buffered saline with an average error of 4 mg/dL while the reference error is 2.5 mg/dL. In single donor serum, the average prediction error is 8 mg/dL while the reference error is 2.5 mg/dL. In multidonor human blood serum the average error is 18 mg/dL while the reference error is 8 mg/dL. Other blood analytes such as albumin, total protein, cholesterol and triglyceride have also been measured.

Thesis Supervisor: Michael S. Feld
Title: Professor of Physics

Acknowledgments

Many people deserve credit for this research, and I would like to take this chance to thank them. First of all, I would like to thank my thesis supervisor, Michael S. Feld, for the opportunity to participate in this exciting research and guiding all aspects of this research. I also thank my academic advisor, Derek Rowell, for guiding my graduate studies in the mechanical engineering department. I also thank Irving Itzkan, the guru, for his brilliant ideas. I thank Ramachandra Dasari for equipment. Andrew Berger played a key role in many parts of this research. Without his contributions, most of this thesis work would not have been possible. I thank Gary Horowitz, a clinical pathologist at Beth Isarael Deaconess Medical Center (Boston, MA) for providing samples and medical information. I also thank Geurt Deinum for ideas in system aligning and flow cells. I thank Ramasamy Manoharan, Eugene Hanlon, and Kyungwong An for advice and information. I thank Carlos Lima for teaching me advanced machining techniques. I thank Katrin Kneipp for providing colloidal solutions and ice cream.

On a personal level, I thank members of the Spectroscopy Laboratory, past and present, for providing moral support and encouragements. In particular, I thank Karen Shafer and Jason Motz for introductions to American culture and English. I thank Nada Boustany for advice.

I thank my friends for lightening my life in Boston. I thank members of the Korean Graduate Student Association. I especially thank Kazunori Tanaka for everything.

Last, but always the best, I thank my parents and brother for their support and love.

This research was funded by Chiron Diagnostics (Medfield, MA) and the National Institutes of Health (Grant No. P41-RR02594), and conducted at the Laser Biomedical Research Center at the Massachusetts Institute of Technology.

Contents

List of Tables

List of Figures

Chapter 1

Introduction

1.1 Background

The transcutaneous measurement of blood analytes is a major challenge. A transcutaneous measurement would not only simplify the blood analysis process, but also is badly needed in applications. Diabetes is one example.

> "Diabetes is a leading cause of death in the United States, and over 16 million Americans are believed to have this disease. In 1992, health care costs to diabetics averaged $2,500 for patient materials such as insulin and needles, plus $11,200 per year treating complications. The total cost of treating diabetes and its complications in 1995, according to the NIH, exceeded $137 billion...
>
> There is tremendous interest ··· in finding a reliable, cost-effective method of noninvasive blood glucose measurement. Annual sales of current blood glucose meters and strips are estimated at $1.2 to $1.5 billion; successful non-invasive technology could dramatically expand this already sizable market."[1]

[1] From the description of the problem by the Research Triangle Institute, http://www.rti.org/technology/nasa-jdf

This is just an example of so many applications for which the transcutaneous measurement of blood analytes can be used. Elimination of painful needle sticking would be welcomed by patients.

With its scientific and engineering challenges, as well as its vast market, this problem has attracted the attention of many researchers in both industry and academia. Many techniques are currently under research, including infrared absorption spectroscopy, electrochemical measurement[20], fluorescence spectroscopy[15], pulsed laser photoacoustic spectroscopy[13], NMR spectroscopy[5], spectral analysis of the chemical components in vitreous humor[19], polarmetric techniques[7], and radio wave impedance.

Most of these techniques, however, have practical difficulties due to the many variables which occur in actual applications, including the presence of other chemical components, change of temperature, and change of optical parameters.

As a first step in solving this problem, we studied blood serum to determine which blood analytes we can measure with our technique, and with what accuracy.

1.2 Why glucose in human blood serum

The selection of glucose as our target chemical has several reasons. As mentioned above, the glucose concentration in blood is a crucial physiological parameter. Only one form of glucose, α-D-glucose, is dominantly found in humans; it can be easily stored as a powder, and is convenient for use in experiments.

Hospital analyzers sample human blood serum. In a blood pathology laboratory, human whole blood is centrifuged to remove blood cells and fibrin before it is analyzed. It is easier to perform measurements without the blood cells, since the presence of blood cells not only changes the optical parameters of the sample thereby affecting the spectrum, but can also allow chemical and biological processes to proceed, therefore changing the chemical concentrations.

1.3 Raman spectroscopy

We have explored the use of spontaneous Stokes Raman spectroscopy to accomplish these ends. Raman spectroscopy gives information about molecular vibrations by measuring the wavelength shift of a photon due to inelastic scattering.

When an incident photon of frequency ω_i is directed on a sample, in most cases a photon of the same wavelength ω_i is emitted.

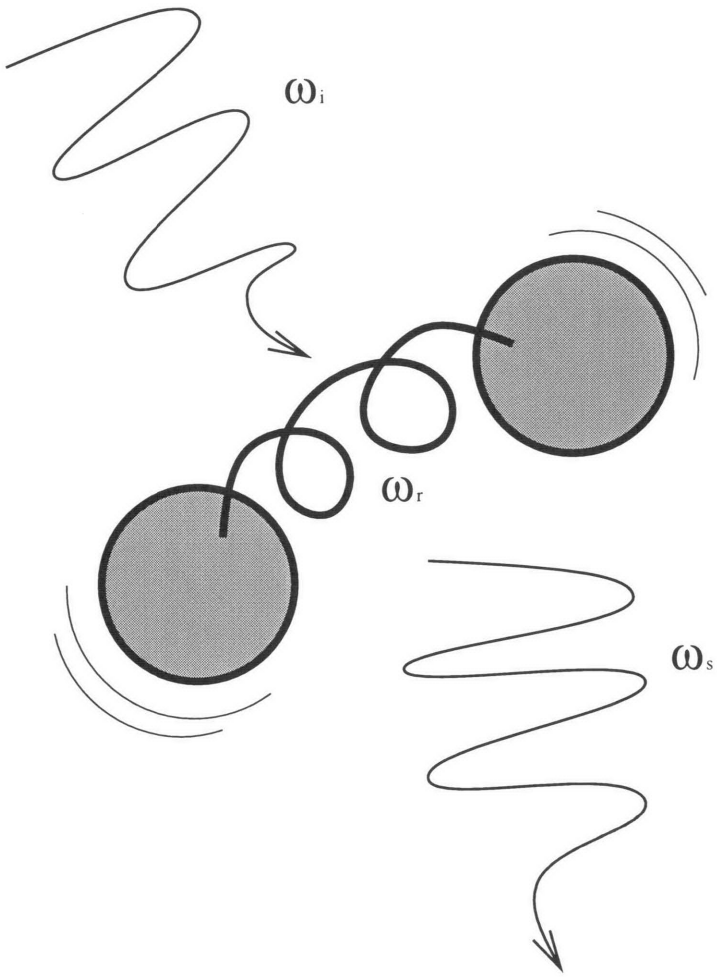

Figure 1-1: Diagram of inelastic scattering effect

In inelastic scattering, the emitted photon has a frequency ω_s, which is different from the frequency ω_i of the incident photon (Figure 1-1). When the frequency shift $\Delta\omega$ equals the vibrational frequency of the molecule, this is called Raman scattering:

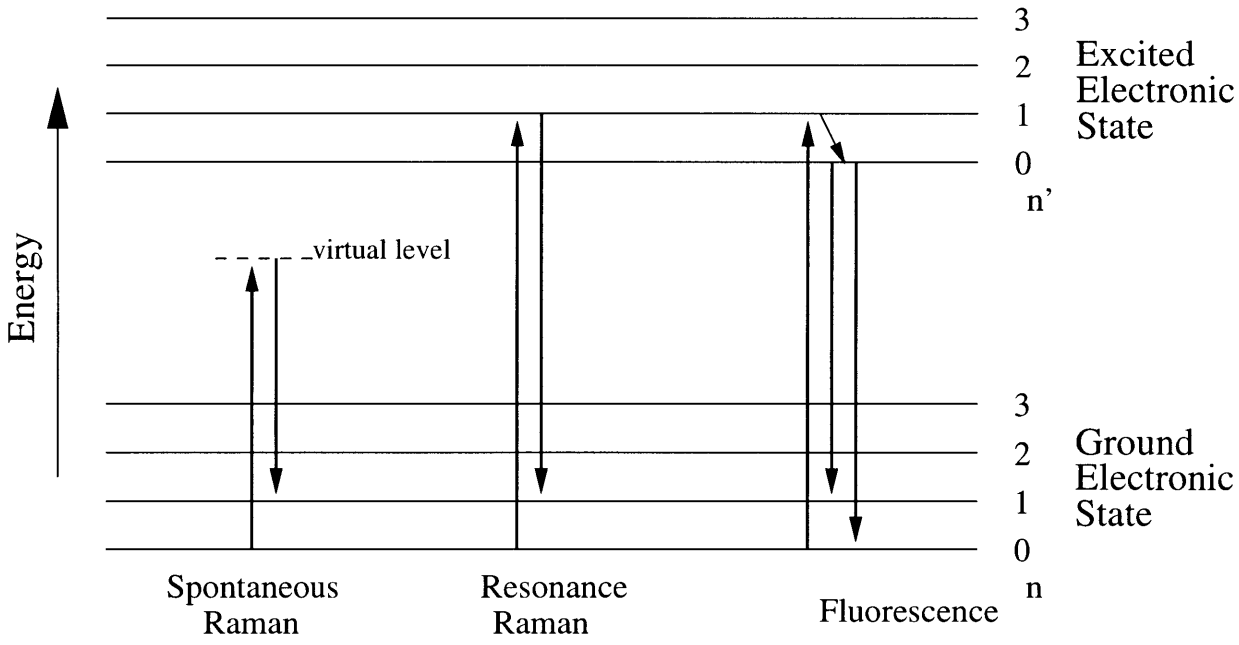

Figure 1-2: Energy level diagram of electronic states in a molecular system. Levels (0, 1, 2, 3, ...) in ground and first excited electronic states are vibrational levels.

$$\Delta\omega = \omega_i - \omega_s.$$

In spectroscopy, the energy of the photon is usually measured in *wavenumbers*.[2] Wavenumber has the unit of inverse centimeter (cm^{-1}), and is proportional to the frequency.[3]

In terms of resonance, Raman scattering is distinguished by whether the scattering is resonant or non-resonant. When the frequency of the incident light equals the frequency of the molecular absorption band, the intensity of the emitted light increases drastically. This is called resonance Raman scattering (RR). Resonance Raman spectroscopy is very useful in cases when a resonance frequency, or absorption band, of the target chemical is known. We, however, do not want any spectrum from one specific chemical to dominate the whole spectrum, because even though we are trying to

[2] $E = hc\tilde{\nu}$, where E is the energy of photons, h the Planck constant, c the speed of the light, and ν the wavenumber.[6]

[3] $\tilde{\nu} = 1/\lambda$, and $\nu = c/\lambda$, where $\tilde{\nu}$ represents wavenumber, λ wavelength, ν frequency, and c the speed of the light.

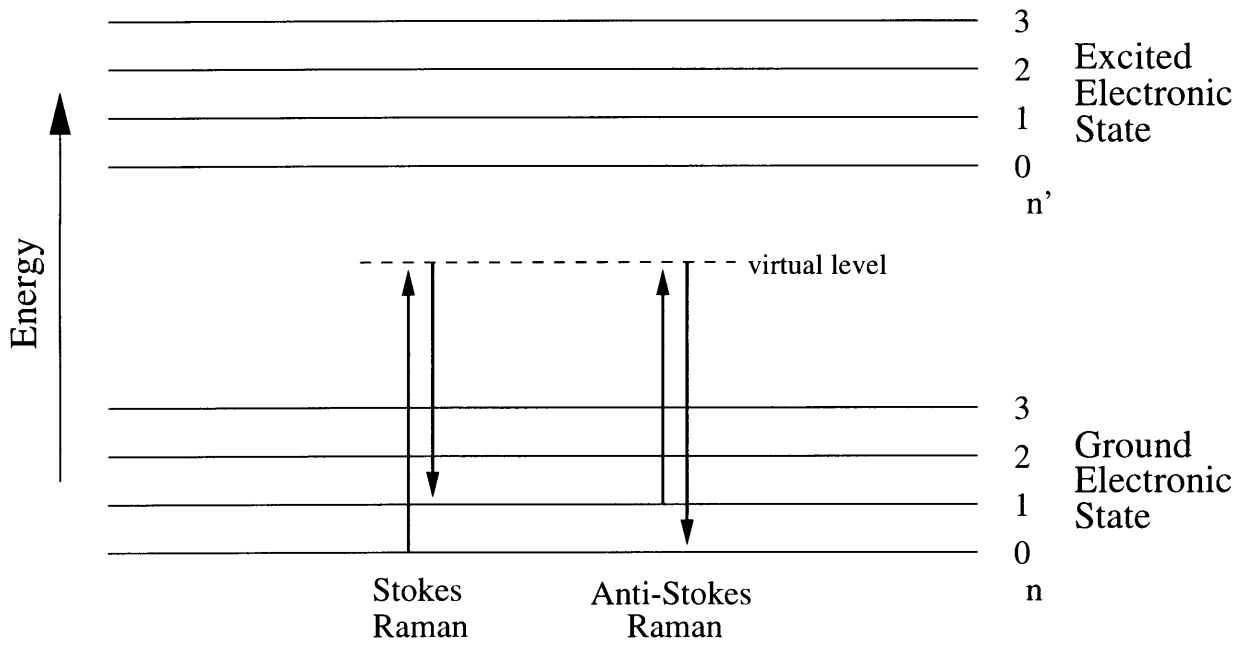

Figure 1-3: Energy level diagram of Stokes and anti-Stokes Raman

measure the concentration level of glucose, we also want this technique to be used for general applications. For this purpose, concentration of chemicals other than glucose is measured in chapter 4. We therefore employ non-resonant Raman scattering, i.e. Raman scattering without resonance, for our studies.

The spontaneous Raman spectrum is a linear combination of the spectrum of each chemical component. This is important in the quantitative analysis, because the linearity allows us to use linear multivariate calibration techniques. This will be discussed in detail in chapter 3.

Raman spectra can be classified according to whether the emitted photon has less or more energy than the incident photon; they are known as Stokes and anti-Stokes Raman spectra, respectively (Figure 1-3). Stokes Raman scattering involves a transition of a photon from the ground vibrational state to an excited vibrational state. Anti-Stokes Raman scattering involves a transition of a photon from an excited vibrational state to the ground vibrational state. As the population of excited vibra-

tional states is very much less than the population of the ground state[4], the signal intensity of anti-Stokes Raman scattering is much weaker than that of Stokes Raman scattering.

One of the disadvantages of Raman spectroscopy is its weak signal. The intensity of a typical Raman spectrum is about 10^{-6} times the intensity of the elastically scattered light. This weakness of signal strength makes detection difficult, especially with huge noise and background. Measuring Raman scattering in the anti-Stokes region can reduce the fluorescence background, because the fluorescence signal is also weaker in the anti-Stokes region. The actual advantage of using anti-Stokes Raman scattering over Stokes Raman scattering, however, should be carefully studied, because it is not guaranteed that the signal-to-noise ratio will improve by using anti-Stokes Raman. Without this knowledge, it is easier to measure the Stokes lines in Raman experiments, because the Stokes signal intensity is bigger than the anti-Stokes signal intensity.

1.4 Excitation wavelength selection

Selecting an optimal excitation wavelength for Raman spectroscopy is very important in studies of biological systems.

There are four issues in selecting the excitation wavelength.

The first one is fluorescence background generation. The signal we are looking for is very small compared with the background. Thus, it is critical to reduce the fluorescence background and its associated shot noise. In biological systems, the shorter the excitation wavelength, the bigger the fluorescence background gets.

The second is the penetration depth. Penetration depth is important in terms of transcutaneous measurement, as well as sampling volume. If the penetration depth is short, the chemical signal we are looking for may be small. We are planning to apply this technique to a transcutaneous measurement, so the penetration depth should be

[4]This is due to the Boltzmann distribution. A molecule is less likely to be present in a higher energy state.[16]

long enough to penetrate the depth of skin. Two major absorbers in the human body are water and hemoglobin.[5] There are some wavelength 'windows' in which the net of absorption of these absorbers is smaller than in other regions.

The third is the intensity of the Raman signal. The intensity of the Raman signal drops as increasing excitation wavelength. [6]

The fourth is the detector sensitivity. The quantum efficiency of a CCD (charge-coupled-device) array drops at longer wavelengths. CCD detectors cut off at about 1.1μm. Thus, as the wavelength of a Raman signal approaches this value, it can be corrupted by readout noise.

We have chosen 830nm as our excitation wavelength. This near infrared wavelength does not generate as much fluorescence background as any shorter excitation wavelength does. 830nm laser light does not resonate with biochemical bonds. There is an absorption 'window' around this 830nm region, so the light can penetrate relatively deep. The Raman signal intensity and the detector sensitivity at 830nm are acceptable for biological studies.[1]

[5]Skin pigments also have a high absorption coefficient.

[6]$I \propto \nu^4$, where I is the intensity of the Raman scattered light, and ν is the frequency of the incident photon.[6]

1.5 Outline

In chapter 2, the experimental system scheme is described. We discuss its basic functions, improvements of the system, and analysis of the system. In addition, suggestions to improve the system in the future are given.

Analytical techniques to extract the chemical concentrations are another main part of these experiments. We have studied and compared alternative techniques and tried to choose the best analysis technique for each analyte. Discussion of feasibility of these techniques and their limits are presented in chapter 3. In addition, reasonable ways to preprocess the spectra, such as spectral range selection and filtering, are discussed.

In chapter 4, we describe in detail three experiments that we performed. The experimental design considerations are given. All the experimental details, including experimental protocols, are fully described. Spectra from each experiment are presented with analysis results.

In chapter 5, the interpretations of the results from the experiments in chapter 4 are given. The same set of spectra has been analyzed by two methods, hybrid linear analysis (HLA) and partial least square (PLS), to compare their performance. In addition, future directions of this project are suggested.

Chapter 2

Experimental System

2.1 System scheme

2.1.1 Overview

The following is a schematic outline of the current system (Figure 2-2 and Figure 2-4). A typical laser spectroscopy system consists of a laser source, delivery optics, collection optics, and a detector. For the laser source, a GaAlAs diode laser is operated at 830nm wavelength in CW mode. The beam is passed through the bandpass filter to remove wavelengths other than the primary wavelength because the laser is oscillating in multi-mode (Figure 2-1). This bandpass filter has a polarization sensitivity, so we checked whether the beam polarization is aligned to the filter axis by comparing the laser power before and after the bandpass filter. The output beam is reflected by two mirrors to ease aligning the system. These mirrors are carefully adjusted to keep the laser beam horizontal. The aligned beam is focused onto the sample by means of a focusing lens. Due to the collection geometry, a reflecting prism is used to bring the beam perpendicular to the sample.

The laser beam impinges on the sample, and interacts with it. Optically, this photon-material interaction produces fluorescence and Raman signals, as well as heat and back-scattered photons.

The reflected or scattered photons are collected by the reflecting objective. The

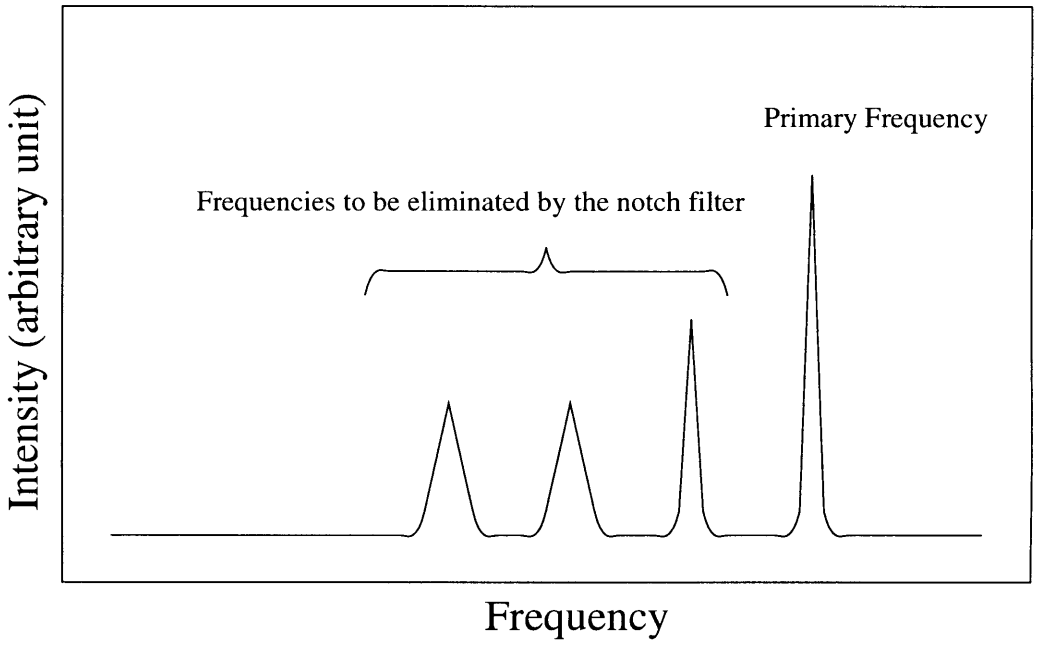

Figure 2-1: Multi-mode operation of the laser. The multi-mode operation of this laser source results from the interaction of the external cavity mode resonances with the resonances of the intracavity mode resonances[18].

reflecting objective has a high numerical aperture (NA) to collect more photons. Light emerging from the reflecting objective is approximately collimated, and passes through the laser line filter to block the laser wavelength. The filtered light is focused onto the input end of the fiber bundle which is arranged in a circular pattern, and transmitted through to the output end. The output end of the fiber bundle is arranged in a linear array (Figure 2-5) which the f-number matching double plano-convex lenses image onto the slit of the spectrometer. Within the spectrometer there is a holographic grating which disperses the light, and the dispersed light is converted to an electric signal by the charge-coupled-device (CCD) camera.

2.1.2 Optical component specifications

Laser source

A GaAlAs diode laser, SDL-8630 made by Spectra Diode Labs, is used as the laser source. The silicon diode laser has some tunability in its wavelength in the near-infrared (NIR) region. This allows flexibility in excitation wavelength selection when combined with appropriate filters and a diffration grating. The power of this laser can vary from 150mW to 500mW without using filters. However, at 830nm wavelength, we found that the laser power can only vary from about 200mW to 400mW. This ability to vary the power output was used for testing the heating of samples, as will be discussed below. The laser source has the following specifications.

Table 2.1: Specifications of the laser source

Operating mode	CW
Operating output power	0.30W
Operating wavelength	830nm
Operating bandwidth	10GHz
Beam Diameter (FWHM)	2mm
Beam Divergence (FWHM)	0.5mrad
Polarization	TE

During the experiment, the average power was kept close to 300mW, and we

observed 3mW power fluctuations by using a laser power meter. This laser has an internal temperature compensating feedback loop to stabilize the laser output against fluctuations in the ambient temperature. This system has an internal interlock for safety purposes.

Delivery optics

In this spectroscopy system, the section which delivers the laser light from the laser source to the sample is called the delivery optics. The delivery optics consists of a holographic bandpass filter, two reflecting mirrors, a focusing lens, and a reflecting prism.

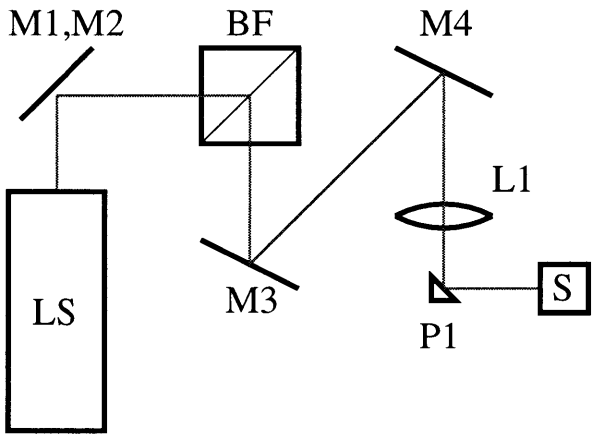

LS: Laser Source
M1, M2, M3, M4: Mirror
BF: Bandpass filter
L1: Focusing lens
P1: Reflecting prism
S: Sample
— : Laser beam

Figure 2-2: Delivery optics

The holographic bandpass filter, Kaiser HLBF-830-1.0, is used in the system to filter out unwanted fluorescence from the laser source. This bandpass filter has a holographic volume grating located between two prisms, and when a collimated and polarized laser beam is directed perpendicular into the cube, some of the unwanted light just passes through the cube, and the rest of the light is diffracted by the grating. By spatially filtering the output beam we could narrow its wavelength, but this is unnecessary because the laser line is narrower than a typical Raman peak from a biological sample.

Table 2.2: Specifications of the holographic bandpass filter

Throughput	$> 90\%$
Wavelength	830nm
Bandwidth	< 2nm
Working angle	90^o
Maximum input power	5W

Two mirrors reflect the output beam from the bandpass filter to simplify the system alignment. When we consider that the laser beam consists of photons moving in the 3D space along a given straight path, the beam has 5 degrees of freedom. A mirror limits 2 of these degrees of freedom, as the mirror changes the angle of the beam. We can direct the laser beam close to a spot where we want it to fall with an angle that is desired using two mirrors.

The focusing lens, Melles-Griot 01LDX 167, collects the light reflected by two mirrors, and focuses the beam to a small spot. The following is the specification of the focusing lens.

Table 2.3: Specifications of the focusing lens

Diameter	22.4mm
Focal length	100mm
Material	BK7
Design wavelength	546.1nm

By combining this information with the information on Table 2.1, we can calculate the focused beam size. First, we need to change the beam width and divergence at FWHM (full width at half maximum) to the beam width and divergence at the $1/e^2$ point. From the intensity distribution of the beam, the beam waist radius $w_0 = 1.7\text{mm}$[1], and the beam divergence $d = 0.3\text{mrad}$[2].

Let us first assume that the laser beam waist is at the front surface of the laser source.[3] Using the focused beam width equation for a Gaussian beam [12],

$$\begin{aligned} s'' &= \frac{f}{1+(\lambda f/\pi w_0^2)^2} \\ &= \frac{100\times 10^{-3}}{1+[\frac{830\times 10^{-9}\cdot 100\times 10^{-3}}{\pi\cdot(1.7\times 10^{-3})^2}]^2} \\ &= 100\times 10^{-3}(m) \end{aligned} \tag{2.1}$$

$$\begin{aligned} w &= \frac{\lambda f/\pi w_0}{[1+(\lambda f/\pi w_0^2)^2]^{1/2}} \\ &= \frac{830\times 10^{-9}\cdot 100\times 10^{-3}/(\pi\cdot 1.7\times 10^{-3})}{[1+\{\frac{830\times 10^{-9}\cdot 100\times 10^{-3}}{\pi\cdot(1.7\times 10^{-3})^2}\}^2]^{1/2}} \\ &= 16\times 10^{-6}(m) \end{aligned} \tag{2.2}$$

where s'' represents the distance from the lens to the focused beam waist, f the focal length of the lens, λ the wavelength of the incident light, w_0 the $1/e^2$ beam width at its waist before the lens, and w the laser beam width at the focused beam waist (Figure 2-3).

According to these equations, the beam is focused at the focal distance of the lens, 100mm from the lens, which is what we confirmed by using an infrared viewer. The diameter of the focused beam is about 32μm in the case of a perfect optics.[4] This is

[1] From the Gaussian beam intensity profile, $w_0/w_{FWHM} = 1.7$, where w_0 is the $1/e^2$ beam width, and w_{FWHM} is the FWHM beam width.

[2] From [17], beam divergence $\alpha = \frac{2\lambda}{\pi w_0}$, where λ is the wavelength of the beam, and w_0 is the $1/e^2$ beam width.

[3] The front surface of the laser source in this case is the output surface of the laser diode chip.

[4] In reality, a lens has aberrations which blur the focused image.

the smallest spot size we can obtain with this focusing lens. However, by changing the focusing lens or the delivery optics configuration, we can get the desired beam width.

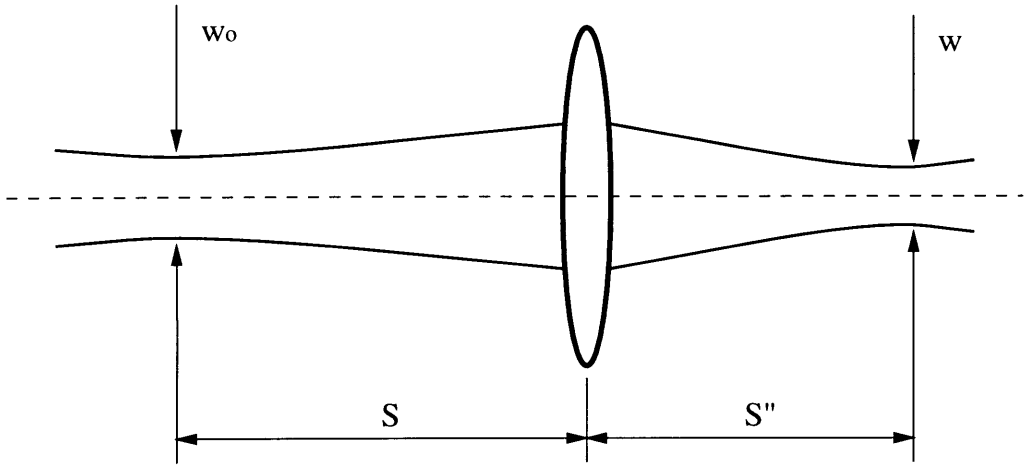

Figure 2-3: Gaussian beam notations

The reflection prism reflects the light focused by the focusing lens. The reflected light is directed onto the sample. The sample absorbs, absorbs and re-emits, or scatters the light.

Collection optics

The collection optics collect the optical signal scattered and/or reflected by the sample and transmits the signal to the detector. The collection optics consist of a reflecting objective, a holographic notch filter, a focusing lens, a fiber bundle, and f-number matching optics.

The reflecting objective is a microscope component that collects light with a very wide viewing angle, which is equivalent to a high numerical aperture (NA). A typical reflecting objective uses two reflecting surfaces. By using two reflecting surfaces, a reflecting objective has two major advantages over a lens in laser spectroscopy. First, a reflecting objective does not produce chromatic aberration. A typical lens is made of transparent material of a certain refractive index such as quartz or BK7. The

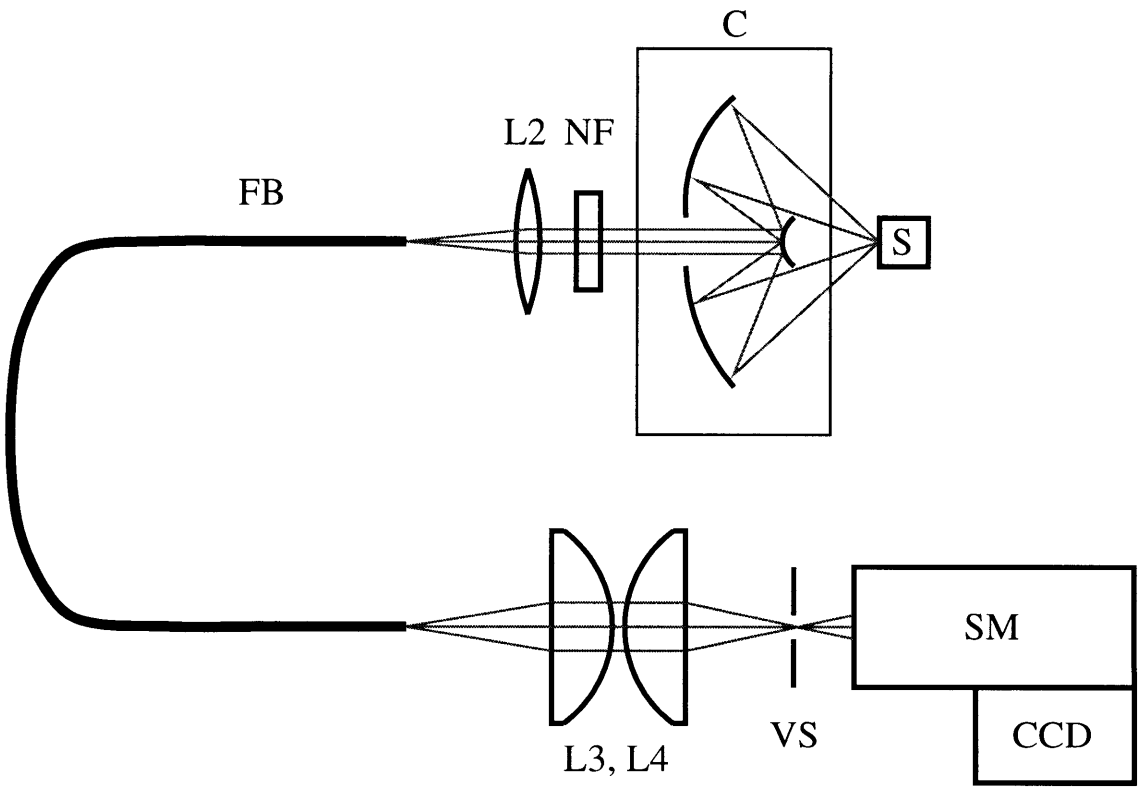

S: Sample
C: Reflecting microscope objective
NF: Notch filter
L2: Focusing lens
FB: Fiber bundle
L3, L4: F number matching optics
VS: Variable slit
SM: Spectrometer
CCD: CCD camera

Figure 2-4: Collection optics

refractive index, however, is a function of the wavelength of the input beam. Thus, a singlet inherently has some amount of chromatic aberration. This aberration problem is discussed in detail below. However, the reflection angle does not change with the wavelength. So there is no chromatic aberration in a reflecting objective. Secondly, in a lens, when the laser beam passes through the medium the lens itself can generate Raman or fluorescence signal. This can be a problem because the added signal can generate additional shot noise. On the other hand, with reflecting surfaces the light does not pass through a medium other than air, which generates almost no Raman or fluorescence signal, so we can avoid the unnecessary signal addition.

Table 2.4: specifications of the reflecting objective

Magnification	x15
NA	0.5
Focal length	13.41mm
Obscuration	19.5 %
Working distance	23.2mm
Reflectivity	> 97% @ 950nm
Coating	Gold

The holographic notch filter, Kaiser HNPF-830-2.0, is used in the system to block the laser line in the collected light. Otherwise, a high power laser beam can saturate the detector, generate additional shot noise, and damage delicate optical components such as the diffraction grating and the detector.

Table 2.5: Specifications of the holographic notch filter

Throughput	> 80%
Wavelength	830nm
Working angle	0^o
Spectral bandwidth	< 599 wavenumbers
Edgewidth (Red side)	121 wavenumbers
Edgewidth (Blue side)	181 wavenumbers
Laser damage threshold	$10J/cm^2$

The focusing lens focuses the collected light onto the end of the fiber bundle. This lens is chosen to match the numerical aperture of the optical fibers.

The fiber bundle is made with 177 optical fibers. At the input end one central fiber which collects most of the light lies in the middle of the bundle. Eighteen fibers form a ring which surrounds the central fiber. 42 fibers form another ring which surrounds the the first ring. 116 fibers form the third ring which surrounds the second ring. At the output end, this fiber bundle transforms the circular beam into a line so that the light can be efficiently coupled into the entrance slit of the spectrometer.

F-number matching optics match the different F-numbers of two components. The light coming out of the fiber has a numerical aperture (NA) different from the numerical aperture of the spectrometer; direct coupling would cause the loss of light. To modify the solid angle of the light and capture all the light, two large plano-convex lenses are used. To minimize spherical aberration, the two convex sides face each other.

Table 2.6: Specifications of the focusing lens

Diameter	100mm
Focal length	120mm @ 546.1nm
Material	BK7

Detector

The detector is the part of this system that transforms the collected light to electric signals. The detector consists of a spectrometer and a CCD camera (Figure 2-4).

The spectrometer disperses the incoming light. This allows us to analyze its wavelength distribution. The Princeton Instrument spectrometer has three lenses, one notch filter and one spectrograph. The first lens collimates the input beam. The notch filter then blocks the laser line. The second lens focuses the beam onto an internal slit, which increases the resolution and filters out some noise. The third lens again collimates the filtered light, and the collimated beam is passed through the grating and dispersed. The dispersed light is collected by the CCD camera. However,

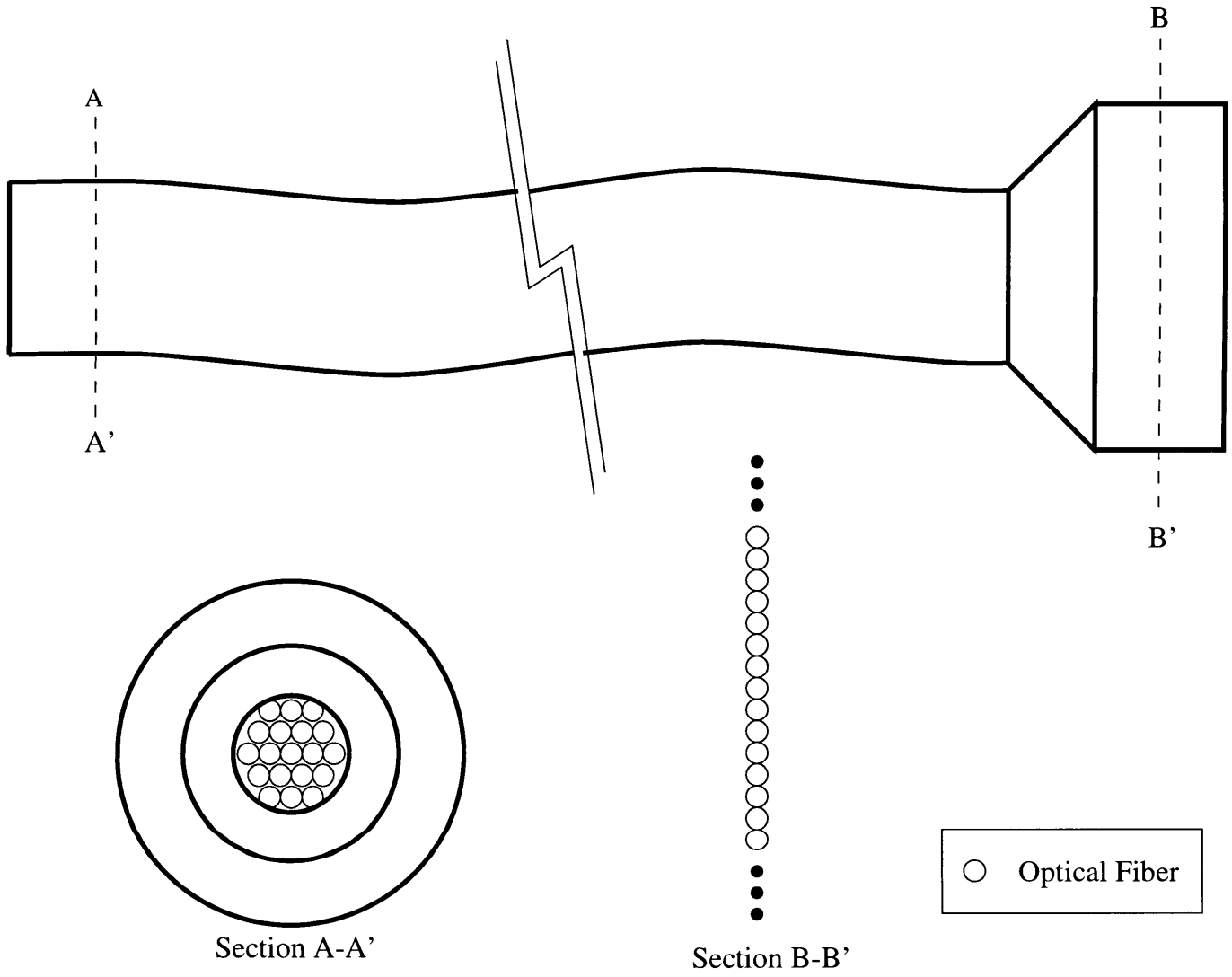

Figure 2-5: Outline of fiber bundle. The input end of the fiber bundle (AA') is circular, and the output end of the fiber bundle (BB') is linear. The fiber bundle has three ringss. Only optical fibers in the center ring are drawn.

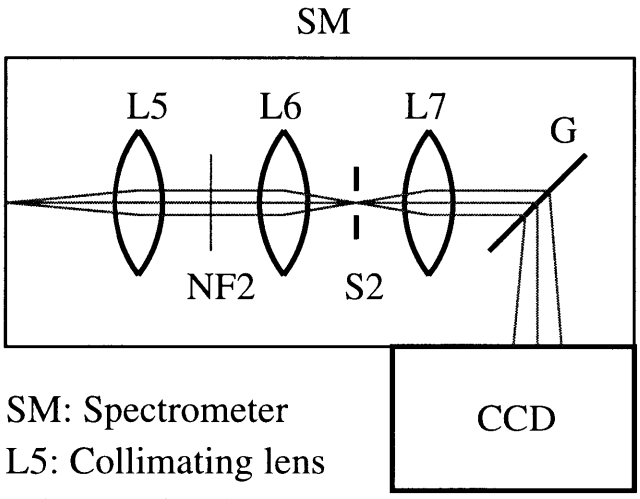

SM: Spectrometer
L5: Collimating lens
L6: Focusing lens
L7: Collimating lens
S2: Slit
G: Dispersion grating
NF2: Notch filter
CCD: CCD camera

Figure 2-6: Spectrometer and CCD

we did not use the notch filter (NF2) and the slit (S2) in our experiments to improve the throughput of the system. Instead, we used an external notch filter (NF) and an external variable slit (VS) (Figure 2-4).

A CCD (charge-coupled-device) array camera is used as a detector. A CCD camera has a higher S/N ratio and lower readout noise than an InGaAs detector [1]. The CCD is already built into an array, from which we get the multiplex advantage. A liquid nitrogen cooled CCD, LN CCD-770HR is used in this system. As the beam is dispersed horizontally by the dispersion grating, the intensity of a specific wavelength component can be measured by counting the number of photons hitting a specific horizontal position on the CCD.

Table 2.7: Specifications of the CCD camera

Number of pixels	1152 x 770
Pixel size	22.5μm

The number of the photons counted for a specific horizontal position is transferred to a controller. The controller stores data in the buffer, and sends it to the computer, which processes the data. The processed data can be displayed as a spectrum, and stored for future analysis by various algorithms.

2.2 System improvements

Besides the major optical components mentioned above, some additions have been devised to solve problems found during preliminary experiments.

2.2.1 Stirring mechanism

During our preliminary studies, we have occasionally observed an abrupt increase of the spectral intensity, along with the weakening intensity of the Raman signal. Figure

2-7 shows this kind of spectral change. Each line in the figure stands for a frame.[5] Because we took 30 spectra of each sample, there are 30 lines in the figure. Each spectrum was gathered for 10 seconds, and the interval between two adjacent spectra was approximately 3 seconds. The first 23 frames remain almost constant except for some cosmic rays.[6] In the 24th frame, the background increased slightly. In the following frames it is obvious that background increased dramatically. Also we find that due to the increased background the shot noise is corrupting the spectrum, as can be seen by comparing the first frame with the last.

In addition, we observed a small black spot on the cuvette wall in these cases. The spot is located at the point where the laser beam is hitting the sample. From this spot, we concluded that damage to the sample caused by heating is happening occasionally. The laser power is 300mW and the beam diameter is 32μm, which gives an average power density[7] of 370MW/m^2. It is conceivable that such high intensities can damage biological samples.

I have devised several ways to prevent or minimize this heat effect. These concepts can be largely classified as passive method and active methods.

Passive method

As the heating is due to the high laser power, we can simply reduce the heat effect by lowering the laser intensity. The advantage of this method is that it is very simple. The disadvantage is that reducing the laser power reduces the signal from the sample. As the signal-to-noise ratio (S/N) is a crucial factor with multivariate prediction techniques [3], we must extend the integration time by a factor of 10 if the laser power is reduced by a factor of 10. This extended integration time is not feasible for practical applications.

---

[5]Instead of taking one spectrum for 300 seconds, we took 30 spectra for 10 seconds each. Each 10 second spectrum is called *a frame*.

[6]In chapter 3, cosmic rays and removal will be discussed in detail.

[7]Average power density = $\frac{power}{area}$

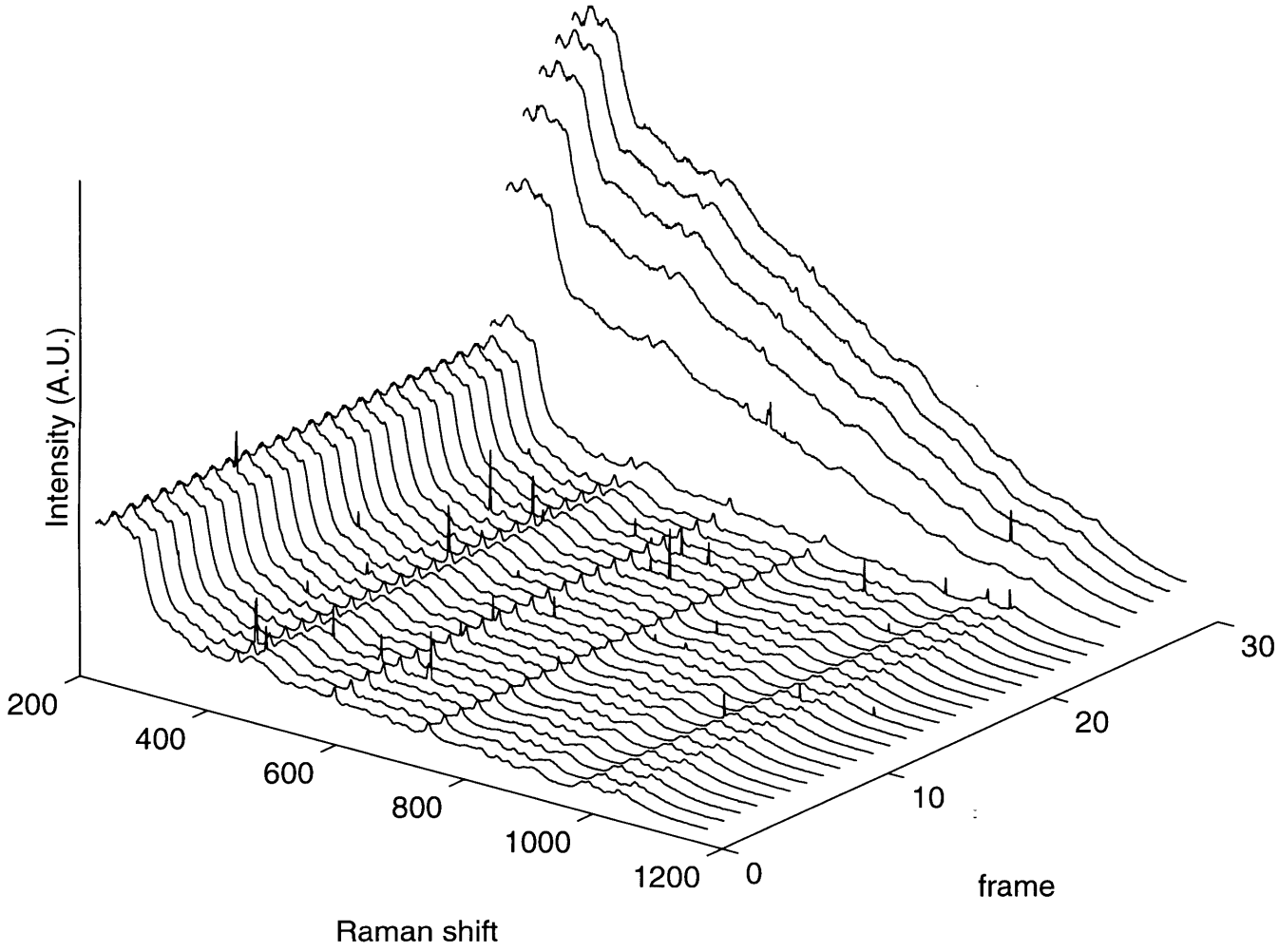

Figure 2-7: Abrupt change in the spectrum due to the heating of a sample

Active methods

Several active methods were considered. These include a flow cell, a moving cell, a stirring mechanism, and temperature control.

The flow cell generates a flow of the sample inside the cell by gravity and/or pressure generated by a pump. The flow cell requires an adequate amount of the sample to circulate. Also, it takes more time to clean and maintain the system after each sample has been used. Possible splash of the biohazard sample is also a problem.

The moving cell moves in translation, rotation, or both. The sample inside the cell moves along with the cell, with some inertia. Sealing is important in this method.

The stirring mechanism is a system with an external part that generates a rotating magnetic field and an internal part, a magnet, that actually spins inside the sample to create a vortex flow. The advantage of this system is that we can incorporate this mechanism into a conventional spectroscopic system with ease. However, the activity of the spinning magnet should be checked to confirm its functioning every time it is used, because the spinning magnet sometimes stalls due to reasons such as geometry and interference of the magnetic field.

Temperature control uses thermo-electric components to sense and control the temperature of the sample in a feedback loop. It is doubtful whether this temperature control can prevent local heating.

After considering all these concepts, we chose a stirring mechanism, which was an improved version of an earlier, inadequate stirring mechanism.

2.2.2 Variable stop

Within the system, the optics which matched the fiber bundle to the f-number of the spectrometer required a compromise. To capture all the light with low f-number optics we had to use large diameter lenses. However, a well-corrected large diameter lens is very expensive, and within the budget, a more affordable lens pair was used. This resulted in some spherical aberration, in addition to chromatic aberration and higher order aberrations.

The chromatic aberration is due to the index of refraction change of glass as a function of wavelength. Therefore the focal length of a lens is a function of the index of refraction[8]

The index of refraction changes from the s line[9] (852.1nm) to the t line (1014.0nm), which is approximately the region that we are using. The refractive index of BK7 is 1.51289 at the s line, and 1.50731 at the t line[14]. The change in focal length, Δf is then given by:

$$\begin{aligned} \frac{\Delta f}{f} &= \frac{\Delta(N-1)}{N-1} \\ &= \frac{N_s - N_t}{N_t - 1} \\ &= \frac{1.50981 - 1.50731}{1.50731 - 1} \\ &= \frac{0.00250}{0.50731} \\ &= 0.005, \end{aligned} \tag{2.3}$$

where f is the focal length of the lens, N the refractive index, N_s the refractive index of BK7 at the s line, and N_t the refractive index of BK7 at the t line.

Thus each lens has a 0.5% change in its longitudinal focal length from the s line to the t line due to chromatic aberration, which is negligible.

The spherical aberration is due to the spherical shape of the lens surfaces. The ideal surface for a lens is not a spherical surface but a more complex aspheric shape. Using the equation for longitudinal spherical aberration [12],

$$\Delta f = \frac{kf}{f/\#^2} \tag{2.4}$$

[8]For a lens in air, $\frac{1}{f} = (N-1)[\frac{1}{R_1} - \frac{1}{R_2} + \frac{t(N-1)}{R_1 R_2 N}]$, where f is the focal length of the lens, N is the refractive index of the lens material, t is the thickness of the lens, and R_1 and R_2 are radii of the curvature of front and back surface of the lens.[17]

[9]*Line* refers to a spectral line in a gas, and is commonly used to designate a specific wavelength in lens design. The s line is the infrared cesium line, and the t line is the infrared mercury line[14].

$$= \frac{0.272 \cdot 120 \times 10^{-3}}{1.2^2}$$
$$= 22.6 \times 10^{-3}(m),$$

where Δf is the change of the focal length, k is the shape factor of the lens in a spherical aberration, f is the focal length of the lens, and $f/\#$ is the f-number of the lens.

The third order spherical aberration in each lens is about 23mm, which cannot be neglected considering its focal length, 120mm.

This aberration creates a blurred image at the spectrometer, and results in a lower resolution of the system. To prevent this aberration from degrading resolution, we built a variable stop. This stop is actually a slit made with two razor blades, each mounted on a micro-positioning stage. These two stages are on one base. We can change the slit width from about 50μm to 5000μm with a repeatability of approximately 1.5μm. This is adequate for our experiments.

This slit allows a higher resolution at the expense of reduced incoming light intensity. A ray tracing simulation done by a computer indicates that we are losing about half the light due to aberrations with a 150μm slit. Changing these lenses would improve the efficiency of the system.

2.2.3 Cell holder

As mentioned above, the reflecting objective has a focal point with a short depth of field, because it has a very high numerical aperture (NA). This results in the collection efficiency being very sensitive to the position of the cuvette, especially when a turbid sample is used. Previously, the cuvette was positioned against a machine-cut corner, which is very imprecise. To improve the reproducibility of positioning, we installed a cell holder which has a plate spring which always holds the cuvette in the same position.

Chapter 3

Analytic methods

3.1 Multivariate calibration techniques

A typical spectrum gathered from a biological sample is a mixture of many overlapping spectra.[1] Extracting the concentration of one specific chemical component was almost impossible before multivariate calibration methods were devised[11].

3.1.1 OLS

The least squares, or ordinary least square method[2] (OLS) is available when the spectrum of each chemical component is known. The OLS fits the target spectrum with the already known spectra. In many practical cases, not even the presence of every chemical component is known, not to mention the spectrum of each chemical component. Thus, OLS cannot be used for multivariate calibration in many applications.

3.1.2 PLS

The partial least squares[3] (PLS) is an enhanced least square method. PLS requires a calibration set, or teaching set, of data to build a model. The partial least squares

[1] Every spectral contribution, including fluorescence, Raman, and infrared absorption/emission, is additive.

[2] OLS is also called classical least squares (CLS).

[3] OLS and PLS are more explicitly discussed in [8] and [9].

method considers an n data point spectrum as an n dimensional vector. PLS compares this vector with the given chemical concentration level and finds spectral components of the given chemical by means of a recursive algorithm. These vectors, or the calibrated model, can be used for predicting the chemical concentration level, which is unknown, in the prediction set.

3.1.3 HLA

Hybrid linear analysis (HLA) is a multivariate calibration technique developed by our group [4]. The motivation for HLA is that PLS uses just the concentration levels and the spectra to build the calibrated model. In many cases, we know, in addition to the concentration levels and the spectra of the samples, the spectrum of the chemical whose concentration level we wish to determine.

We have shown that when both are compared, HLA predicts chemical concentrations with less error than does PLS[4], so we use HLA for analysis whenever HLA is appropriate (Chapter 4). A comparison of the performance of HLA and PLS is discussed in Chapter 4.

3.1.4 Validity of cross validation

In most of our analyses, cross-validation has been used for calculating the prediction error and generating the overall prediction plot. The "leave-one-out" method is a typical cross validation, which leaves out one data point for calibrating the model and then uses the model generated to predict the value of that data point. For example, when one measures N samples, one needs to repeat the calibration N times to get the prediction, each time taking a different sample as the object to be predicted and the rest of the spectra for calibration (Figure 3-1).

Internal validation, basically, is not as robust as external validation. Cross validation, however, can be accepted when done with close attention and inspection of the calibration model itself. [10, 11] Cross validation maximizes the use of limited data sets.

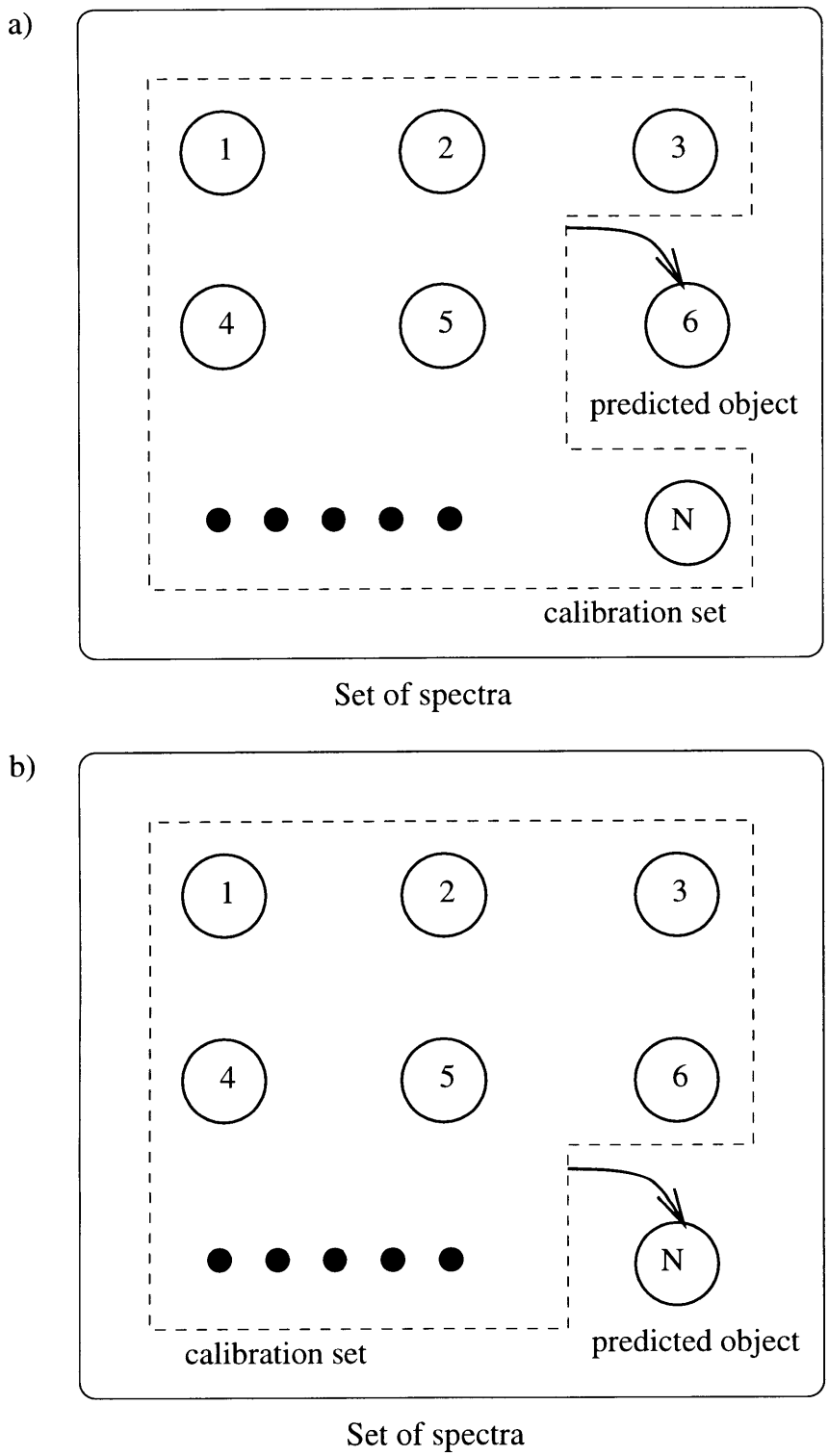

Figure 3-1: How cross validation works. a) To predict a certain concentration in the 6th spectrum, every spectrum other than the 6th spectrum (1, 2, ..., 5, 7, ..., N) is used to build the calibration model, which is then used to predict the concentration of the 6th spectrum. b) For the N-th spectrum, every spectrum other than the N-th spectrum (1, 2, ..., N-1) is used to build the calibration model.

3.1.5 Limits of calibration methods

When one measures some physical value, it is measured in terms of a reference. Unavoidably every concentration measurement has some amount of error in it. Thus every calibration set and prediction set contains measurement error. When the calibration model is built, all the measurement error in the calibration set is averaged out. By increasing the size of the calibration set, we can reduce the measurement error in the calibrated model. There is no way, however, to verify that the calibrated model is performing better than the reference technique, since the measurement error in the prediction set remains in the prediction error:[4]

$$\sigma^2_{apparent} = \sigma^2_{reference} + \sigma^2_{actual},$$

where $\sigma_{apparent}$ is the prediction error value from the analysis, $\sigma_{reference}$ is the measurement error of the reference technique, and σ_{actual} is the prediction error due to the analysis technique and the system.

The error we measure directly from the analysis is $\sigma_{apparent}$, and by knowing the measurement error of the reference technique we can estimate σ_{actual}, the actual prediction error due to the calibrated model.[10]

Based on this, we carefully estimated the measurement error of the reference technique. All the prediction errors presented in this thesis should be kept in mind along with the measurement error of the reference technique.[5]

[4]Even if we have a perfect model, the prediction error would be non-zero because of the measurement error in the prediction set.

[5]However, values of σ_{actual} are not presented in this thesis, because $\sigma_{apparent}$ is not directly comparable with $\sigma_{reference}$. $\sigma_{apparent}$ is an RMSEP (root-mean-squared-error of prediction) value, while $\sigma_{apparent}$ is a CV (coefficient of variation) value.

3.2 Preprocessing

3.2.1 Spectral Range Selection

Multivariate calibration methods mathematically try to find the spectral components that are correlated with the species concentration. With the presence of a strong signal which varies distinctively from sample to sample, the algorithm may try to fit this strong signal, neglecting the variance of other regions. In addition, it is not logical to use a spectral range which does not contain the spectrum of the specific chemical component. With this reasoning, we chose the spectral range that is to be analyzed by the multivariate calibration algorithm. No special algorithm was devised for selecting the optimal spectral range. We iterated, changing the spectral range to minimize the prediction error by a trial-and-error method.

3.2.2 Filtering

The raw data spectra contains several major sources which can degrade the quality of the spectra.

Cosmic Rays

The first source of spectral degradation is cosmic rays. A problem with CCD cameras is that cosmic rays degrade data (Figure 3-4). Cosmic rays hit random pixels of the CCD array with arbitrary intensity.

Some amount of cosmic ray signal can be tolerated for qualitative analysis. One technique of dealing with cosmic rays is increasing the integration time to average cosmic rays out. This method, however, is not feasible for practical applications, because extended integration time can induce the degradation of samples, and long integration times make clinical measurements difficult.

'Averaging-out' is not a good way to treat cosmic rays in a quantitative analysis. The quantitative analysis is sensitive to the intensity of each pixel, and such a huge signal change affects the whole analysis (Figure 3-5). We cannot extract any useful

information from a pixel affected by a cosmic ray.

Our solution for cosmic rays is to remove the cosmic ray signals with software. Taking spectral signals frame by frame enables this filtering. As explained in chapter 2, when we wanted 300 second integration time for a spectrum, we collected 30 spectra of 10 second integration time each. Each spectrum of 10 seconds is called *a frame*. A statistical algorithm was used. The main concept of the cosmic ray filtering assumes the following:

- The spectrum does not change its intensity from frame to frame other than due to noise.
- A sudden change in the spectrum is due to a cosmic ray.

Then we can mathematically express the intensity of one pixel.

$$I = S + \eta + c \tag{3.1}$$

where I is the intensity read by the detector. S represents the average signal including laser, Raman signal and fluorescence. η is the term representing the noise fluctuation, and c is the signal increase due to a cosmic ray.

Once given a statistically feasible number of frames, we can calculate the mean and the standard deviation of the set of pixel intensity in frames. The mean is mostly close to S. The standard deviation is mainly due to the noise η and cosmic rays c. The coefficient of standard deviation is used for deciding what percentile of the pixels are 'normal.' We varied the coefficient of the standard deviation, but mostly used *the mean plus three standard deviations* as the filtering criterion. Any pixel whose intensity is larger than this criterion was replaced with the average of the normal pixels in the other frames.

Cosmic ray filtering has one weakness in its assumption. The variation of the signal in one pixel gets bigger when there is an intensity change of the spectrum over the whole frame due to physical or chemical changes in the sample, such as chemical

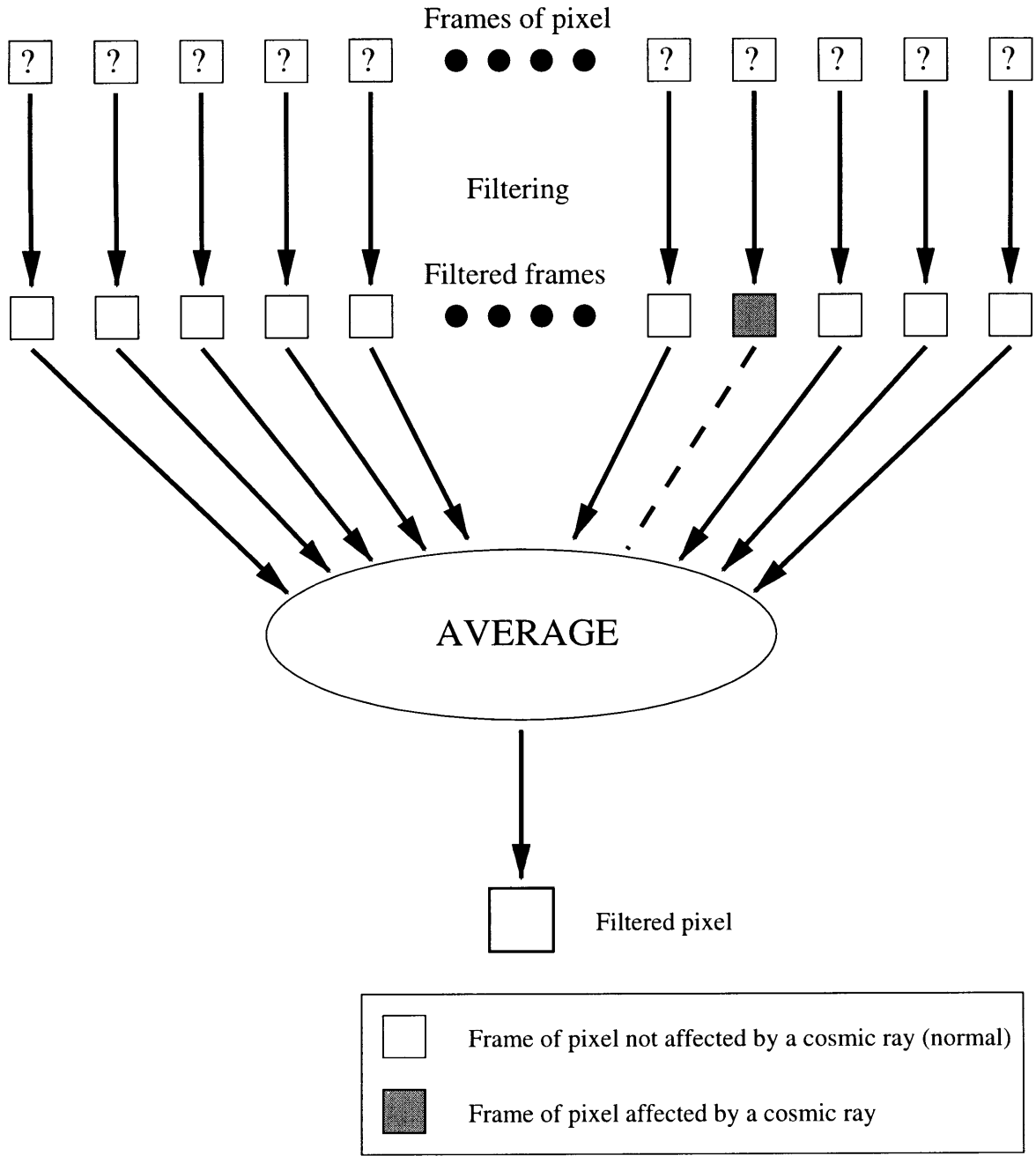

Figure 3-2: The concept of a statistical filter

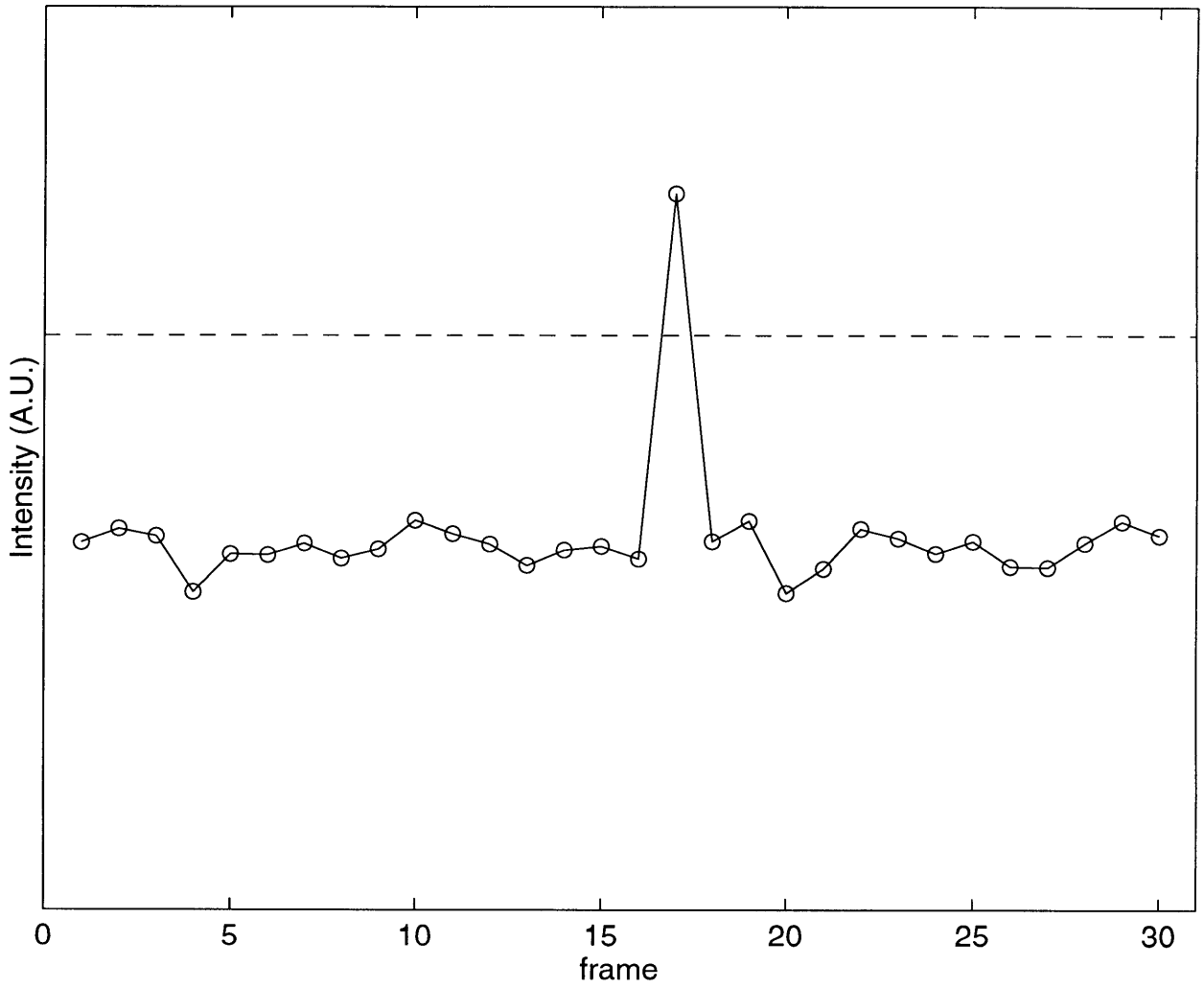

Figure 3-3: The intensity of a certain pixel in frames. The intensity changes due to some noise. The pixel in the 17th frame increased due to a cosmic ray. The filtering criterion is calculated using the mean plus 3 times the standard deviation, and classifies the affected pixel.

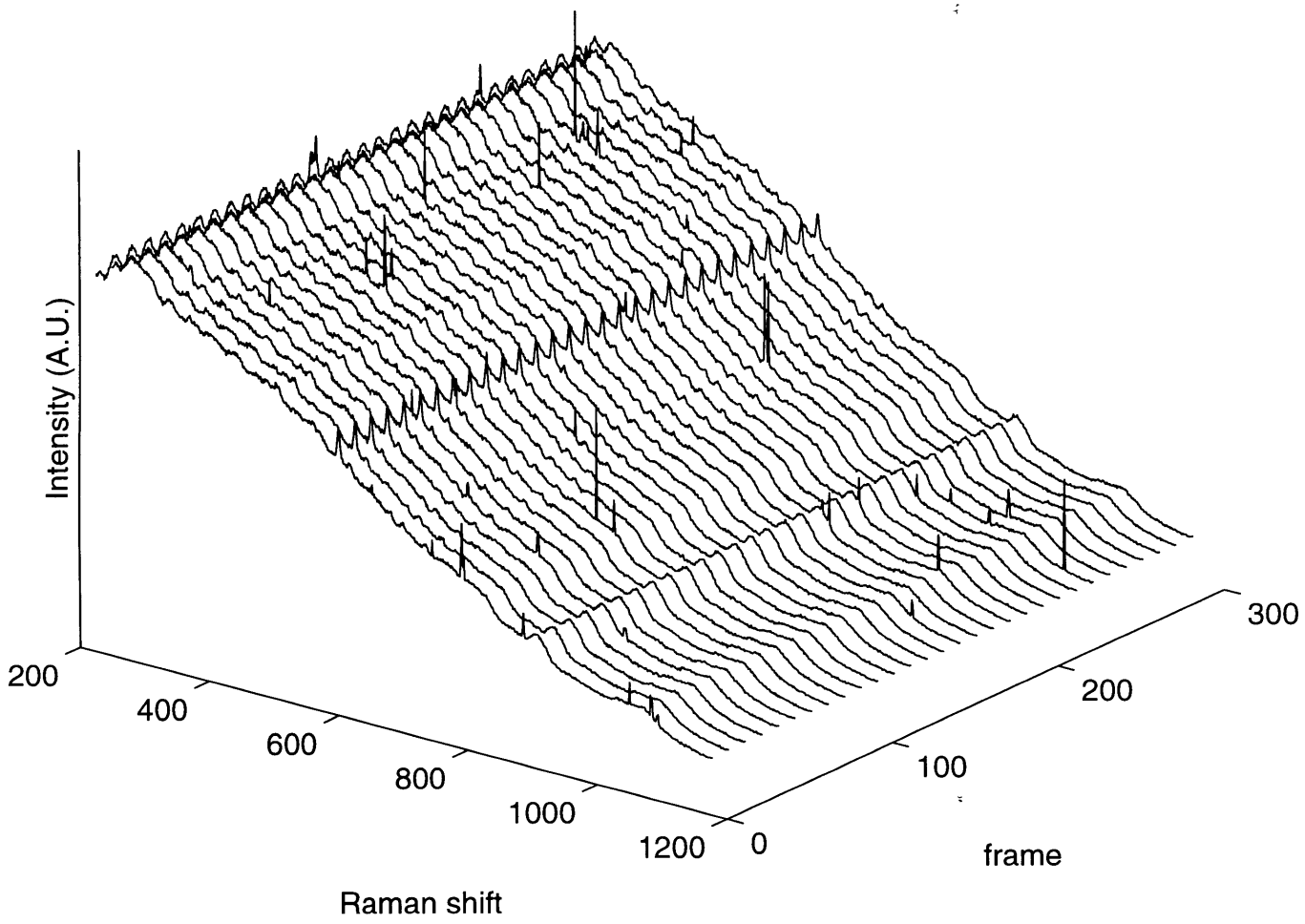

Figure 3-4: A set of raw spectra of a biological sample. Spike shaped peaks are due to cosmic rays.

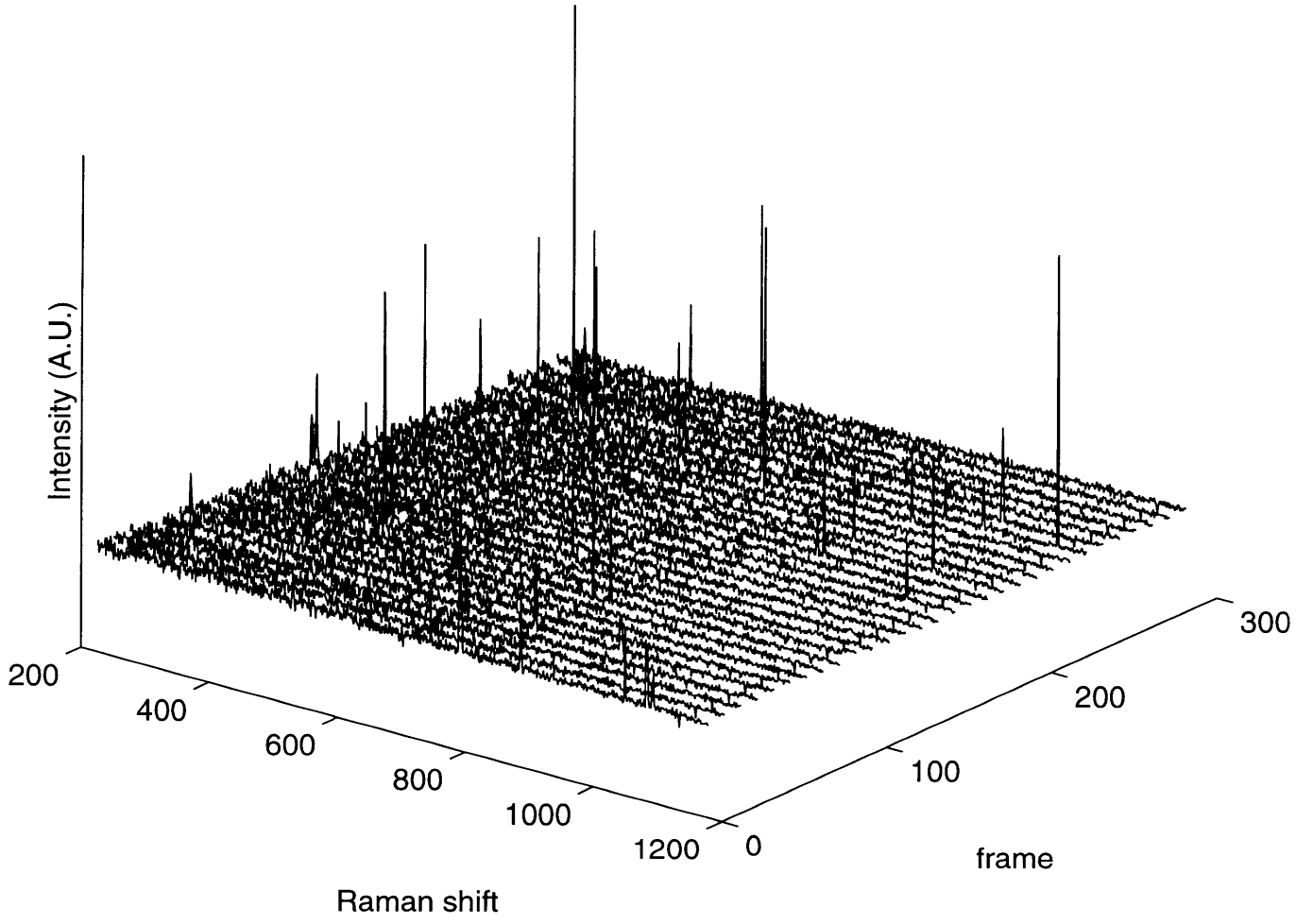

Figure 3-5: A set of spectra of a biological sample. To show the intensity difference between the spectral signal and a cosmic ray, fluorescence background has been removed. Spikes are due to cosmic rays, and Raman signals are the small structure at the bottom.

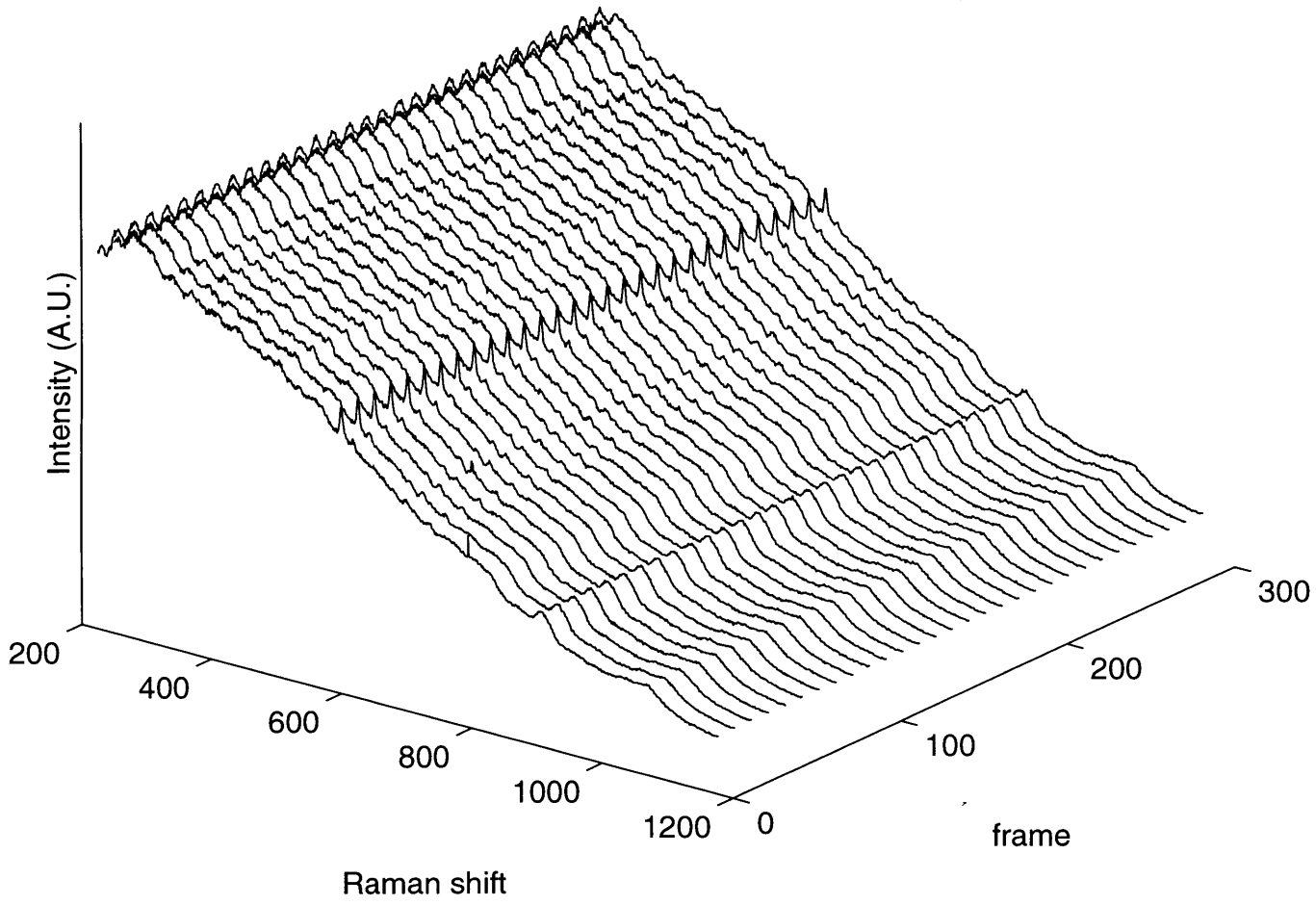

Figure 3-6: A set of spectra of a biological sample with cosmic rays filtered out. A statistical algorithm was used to filter the cosmic ray. Three times the standard deviation was given as the filtering criterion.

breakdown and temperature change. This increased standard deviation may make it difficult to detect cosmic rays by increasing the criteria.

Low S/N ratio

The second source of spectral degradation is low signal-to-noise ratio. A typical Raman spectrum of serum has not only a high fluorescence background, but also a high level of noise, mostly due to the shot noise of the background. Approximately, the ratio among the signal, noise and the background is 1:6:800 (Figure 3-7). Our analysis techniques (PLS and HLA) can overcome a high fluorescence background, but still a low signal-to-noise ratio is a problem, because the prediction error in these prediction techniques increases with the noise corruption of the signal[3]. By averaging several adjacent pixels, we improved the signal-to-noise ratio at the expense of reducing the uniqueness of the spectrum.

Shifting

The third source of spectral degradation is spectral line shifts. Most optical parameters are functions of temperature. The performance of optical components vary with temperature. The laser source and the CCD camera have closed-loop feedback control systems to compensate for temperature changes. However, all the other parts of the system, including lenses, mirrors, and even the sample can be affected by a temperature change. Lenses change their focal length, and the grating changes its dispersion. The experiments are performed in an air-conditioned room. This room, however, was not designed for temperature sensitive experiments. The effect of the temperature change can be easily observed with the spectrum. We observed the shifting of the spectrum by less than one pixel, which is equivalent to 4 wavenumbers. This amount of shift is acceptable for a qualitative analysis. However, a computerized algorithm for a quantitative analysis can be highly affected by this shift. By binning, we solved this problem, again at the expense of reducing the rank of the spectrum.

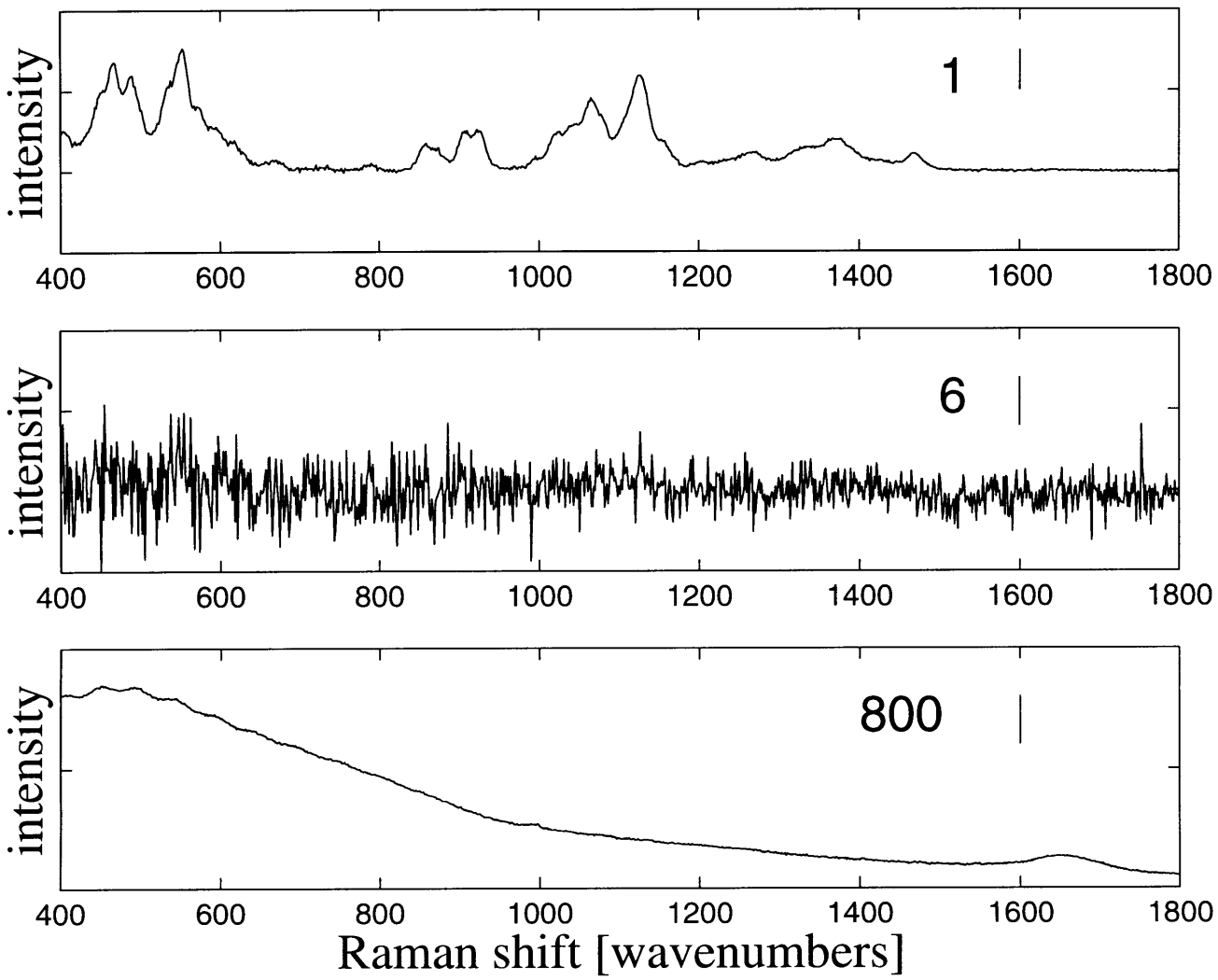

Figure 3-7: Comparision of the size of the signal, noise, and the background in a typical serum sample. $10mg/dL$ glucose spectrum is used as a signal. Noise is shot noise of the background. The integration time is 300 seconds.

Chapter 4

Experiments

4.1 Experiment design

Sets of three experiments were designed using a step-by-step approach. First, we did a phosphate buffered saline experiment to study the feasibility of the Raman technique and the performance of the system. Then we moved to biological samples with controlled chemicals. Finally, we measured the chemical concentrations in human blood serum samples from multiple patients, in which many chemicals vary from sample to sample.

4.2 Glucose in phosphate buffered saline experiment

We first measured the glucose concentration level in phosphate buffered saline (PBS) solution. PBS generates low fluorescence background, and has very low turbidity. The low background level is equivalent to a high signal-to-noise ratio, because a large background generates large shot noise. The low turbidity results in low absorption, which creates less heating problem. The goal of this experiment was

1. to see if we can measure the glucose concentration over the expected range in humans in a very simple solution.

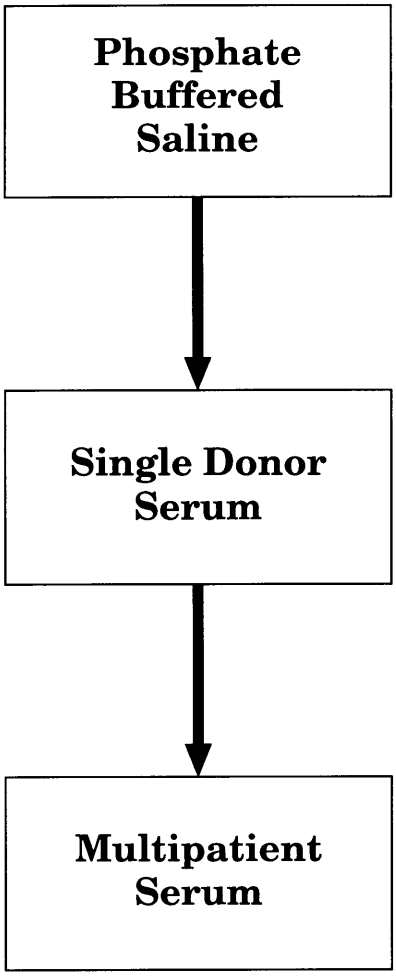

Figure 4-1: Experimental phases for the serum experiments

2. to evaluate the system performance.

3. to compare the performance of PLS and HLA.

4.2.1 Experimental procedures

The samples were prepared in the following way (Figure 4-2). First, a batch of phosphate buffered saline was prepared. This solution was divided into two parts, one of which was doped with glucose to make the concentration 20mM. This glucose doped saline was mixed with saline without glucose at different ratios to generate 21 samples of different glucose concentration levels from 0mM to 20mM in 1mM step (Table 4.1).

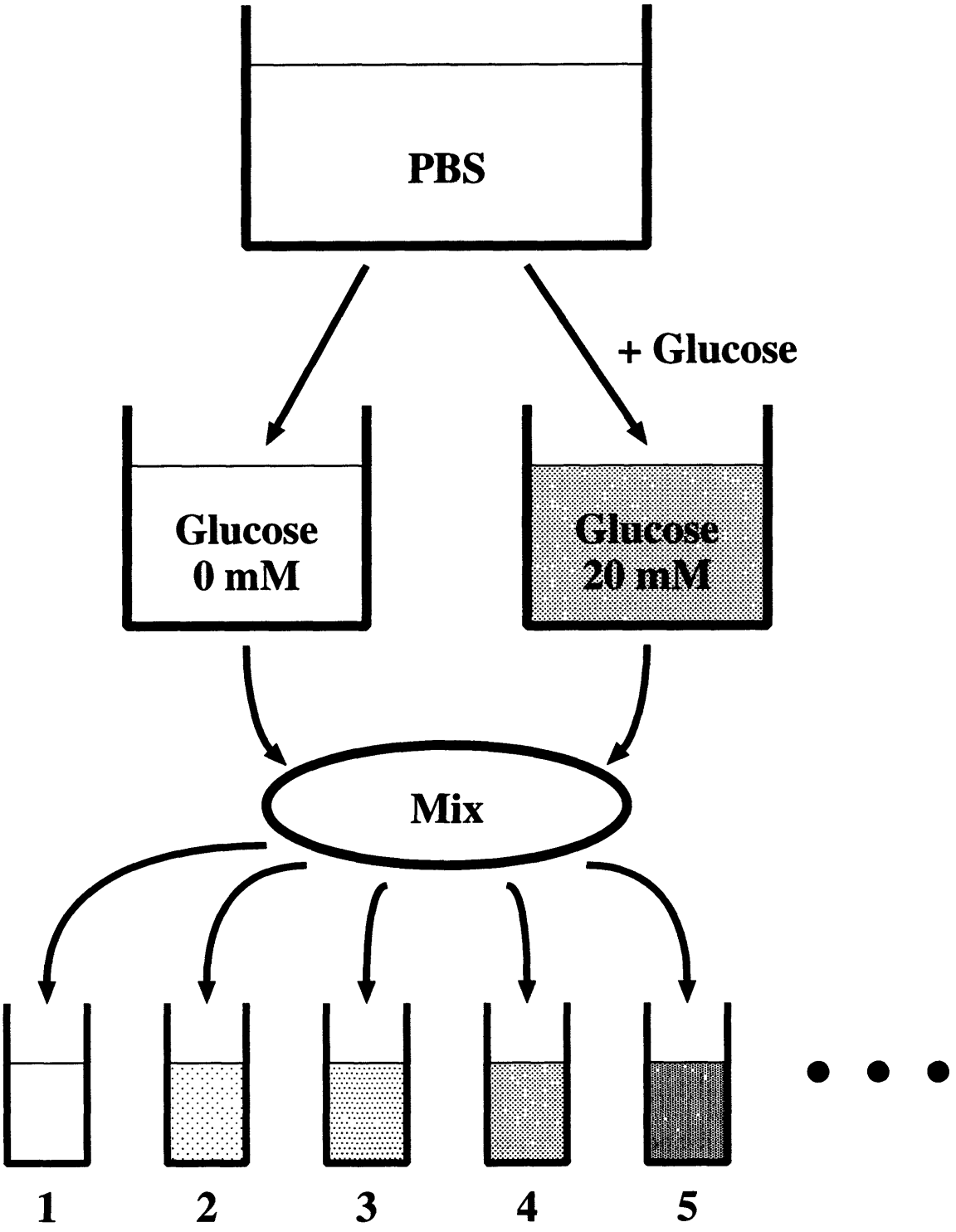

Figure 4-2: PBS sample preparation protocol

Table 4.1: Sample preparation recipes in concentration controlled experiments

Glucose concentration (mM)	20mM glucose batch (μl)	0mM glucose batch (μl)	Estimated concentration error (%)
0	0	2000	0.00
1	100	1900	1.17
2	200	1800	1.00
3	300	1700	1.17
4	400	1600	0.99
5	500	1500	0.87
6	600	1400	1.00
7	700	1300	1.17
8	800	1200	0.99
9	900	1100	1.17
10	1000	1000	0.34
11	1100	900	1.17
12	1200	800	0.99
13	1300	700	1.17
14	1400	600	1.00
15	1500	500	0.87
16	1600	400	0.99
17	1700	300	1.17
18	1800	200	1.00
19	1900	100	1.17
20	2000	0	0

The concentration error in these samples was mostly due to the pipetting error. The concentration errors in Table 4.1 were calculated using the error of the pipette given by the manufacturer. Concentration error was approximately 1% in each sample, and this will be presented as the reference error in the future.

Each sample was contained in a quartz cuvette, and brought to the system for measurement. Once the cuvette was held in place by the holder, the stirring magnet mechanism was turned on. After the spinning of the magnet was checked, the laser beam irradiated the sample, and the spectrum was taken for 200 seconds (20 frames of 10 second integration time). The laser power in this experiment was 300mW.

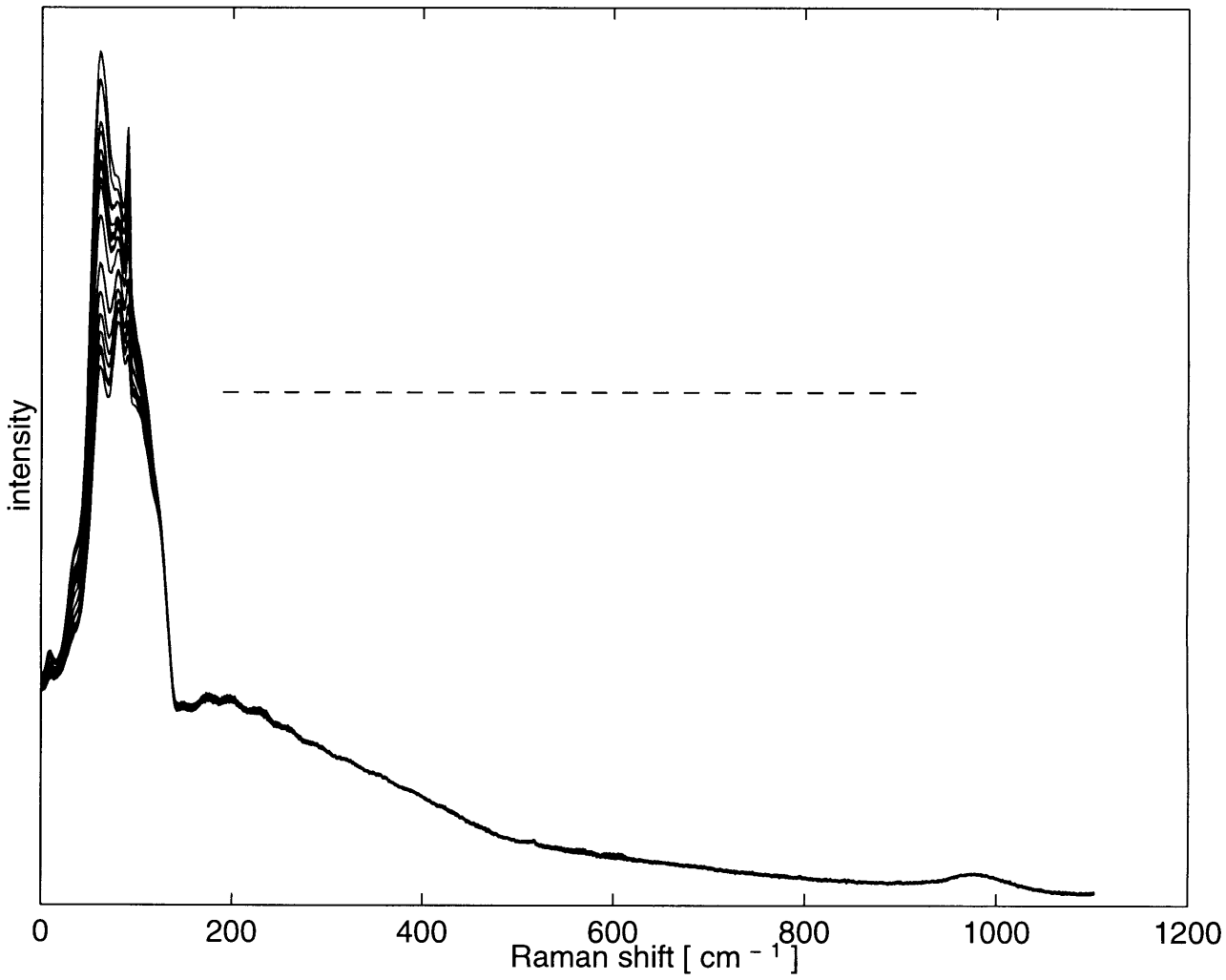

Figure 4-3: Spectra of 21 phosphate buffered saline (PBS) samples

These spectra (Figure 4-3) almost overlap one another. The variation of the peak

intensity in the left side is due to power fluctuation in the reflected and scattered laser light, because of minor changes in geometry from sample to sample. This is not due to any chemical component. The dashed line indicates the region used for analysis. No significant Raman signal from glucose can be observed by eye on this scale.

4.2.2 Measurement of Glucose

As glucose is a simple chemical, we can easily obtain its Raman spectrum. With this spectrum known, we used HLA for predicting the glucose concentration.

Figure 4-4 is the prediction plot of glucose concentration in phosphate buffered saline. The x-axis represents the concentration measured by 'the reference technique', and the y-axis represents the concentration predicted by the HLA algorithm.

The reference error in the experiment is 2.5mg/dL[1], whereas our prediction error (root-mean-square-error-of-prediction, or RMSEP) is 4mg/dL. The correlation coefficient r is 0.999. We conclude that most of our prediction error came from the error of the sample preparation technique, pipetting, and that the accuracy might actually be higher than the reference technique.

This result is very promising. We conclude that the Raman technique is feasible, and the system works without any major problems.

4.3 Single Donor Blood Serum Experiment

We next measured the glucose concentration level in single donor blood serum, which is whole blood with the blood cells and fibrin removed. Blood serum is what a hospital uses for blood analysis, and thus is of interest. Serum generates a high fluorescence background, and has low turbidity. The low turbidity results in low absorption, which generates less heat. The high fluorescence background, which is one of the differences from the PBS experiment, generates more shot noise. This noise affects

[1]There are two units of concentration used in this thesis, molarity and density. The molar unit M is more conventional in chemistry, while density units such as mg/dL or g/dL are more conventional in medicine. For glucose $1mM = 18mg/dL$

the measurement by reducing the signal-to-noise ratio. The goal of this experiment was to check whether our Raman technique can work with biological samples even with these difficulties.

4.3.1 Experimental procedures

Blood serum from about 40 patients was gathered at the Beth Israel Deaconess Medical Center. After collection all samples were kept at 4^o Celsius in a sterile air-capped environment until processing. All the serum was mixed to produce a single batch of serum so that the mixed serum has the general composition of human blood serum and homogeneity, but does not have any specific characteristics of a single donor. This batch of blood serum is equivalent to a single donor serum whose chemical concentrations have average values.

The samples were prepared as follows (Figure 4-5). First, a batch of human blood serum was prepared. This batch was divided into two, one of which was doped with glucose to a concentration of 20mM. This glucose-doped serum was mixed with serum without glucose in different ratios to generate 21 samples with different glucose concentration levels from 0mM to 20mM with 1mM step (Table 4.1). The reference error in this experiment was due to pipetting error, which is the same as in the PBS experiment.

The laser was operated at the same power as in the PBS experiment, 300mW.

All the experimental procedures were identical to the experimental procedures of the PBS experiment except the following:

- We followed biohazard experimental handling procedures in this experiment.
- The total integration time for each spectrum was 300 seconds.

These spectra (Figure 4-6) somewhat overlap one another, but have more variability than the PBS spectra (Figure 4-3). Sample degradation can be a cause to change this spectral variation. Also, when we prepared samples from a batch of human blood serum, inhomogeneity of the serum from sample to sample could have occurred.

4.3.2 Measurement of Glucose

Figure 4-7 is the prediction plot of glucose concentration in single donor serum. The x-axis represents the concentration measured by 'the reference technique', and the y-axis represents the concentration predicted by the HLA algorithm.

The reference error is 2.5mg/dL, whereas our prediction error (RMSEP) is 8mg/dL. The correlation coefficient r is 0.997. This prediction error is less than the acceptable error set by our clinical pathologist.

4.4 Multipatient Blood Serum Experiment

We next measured the blood analyte concentrations, including the glucose concentration level in multipatient blood serum. Again, blood serum generates high fluorescence background and has low turbidity. The difference between this experiment and the single donor blood serum experiment is that there are other chemical components that vary arbitrarily from sample to sample. These variations make the analysis more difficult, because a change in the spectrum may or may not be due to a specific chemical component that we are measuring. The goal of this experiment is to check whether our Raman technique can work with biological samples even with these difficulties.

4.4.1 Experimental procedures

Blood serum samples from 29 patients were gathered at the Beth Israel Deaconess Medical Center. All the serum samples were analyzed with a Hitachi blood analyzer at the BID Medical Center in advance. Each sample drawn from the human body was stored at 4°C in a sterile air-capped environment until it was processed. Sodium fluoride and heparin were used to prevent coagulation and glucose break-down due to the red cells. Every sample was kept at room temperature for approximately the same time to prevent condensation on the cuvette surface and keep each sample at the same temperature. Each spectrum was integrated for 300 seconds at the laser power, 300mW.

These spectra (Figure 4-8) shows more variation than the single donor blood serum spectra (Figure 4-6). This can be mainly due to different chemical concentrations in samples from different patients. One might also guess that it is partly due to the temperature change effect. Even though each sample was kept at room temperature for about the same time, the actual length of time was not always the same. However, we could not keep samples at room temperature for extended time period to make sure that the temperature of samples is same as room temperature, because not only sample degradation but also chemical changes can occur at room temperature. Differences of the sample temperature might produce differences in the optical parameters of the sample such as the absorption coefficient(μ_a) and the scattering coefficient(μ_s'). These changes in optical parameters possibly change the shape of the background.

The reference error in this experiment is the measurement error of the hospital blood analyzer.

4.4.2 Measurement of Glucose

Figure 4-9 is the prediction plot of glucose concentration in multipatient serum. The x-axis represents the concentration measured by 'the reference technique', and the y-axis represents the concentration predicted by the HLA algorithm.

The reference error in the experiment is 8mg/dL, whereas our prediction error (RMSEP) is 18mg/dL. The correlation coefficient r is 0.87. This prediction error is about that which a clinical pathologist would require.

4.4.3 Measurement of other blood analytes

Using the same set of data, we measured the concentration levels of blood analytes other than glucose.

Figure 4-10 is the prediction plot of *albumin* concentration in multipatient serum. The x-axis represents the concentration measured by 'the reference technique', and the y-axis represents the concentration predicted by the PLS algorithm.

The reference error in this experiment is 0.12g/dL, whereas our prediction error

is 0.16g/dL.

Figure 4-11 is the prediction plot of *total protein* concentration in multipatient serum. The x-axis represents the concentration measured by 'the reference technique', and the y-axis represents the concentration predicted by the PLS algorithm.

The reference error in this experiment is 0.17g/dL, whereas our prediction error is 0.22g/dL.

For total protein and albumin, we are limited by the error of the reference technique, and we may have exceeded the accuracy of the reference technique.

Figure 4-12 is the prediction plot of *cholesterol* concentration in multipatient serum. The x-axis represents the concentration measured by 'the reference technique', and the y-axis represents the concentration predicted by the PLS algorithm.

The reference error in this experiment is 5mg/dL, whereas our prediction error is 16mg/dL.

Figure 4-13 is the prediction plot of *triglyceride* concentration in multipatient serum. The x-axis represents the concentration measured by 'the reference technique', and the y-axis represents the concentration predicted by the PLS algorithm.

The reference error in this experiment is 4mg/dL, whereas our prediction error is 37mg/dL.

4.5 HLA vs PLS

In order to establish that HLA generates lower root-mean-square-error-prediction (RMSEP) than PLS, sets of spectra gathered in PBS, single donor serum, and multipatient serum experiment were analyzed using both HLA and PLS, and the results compared.

Figure 4-14 indicates that lower RMSEP's have been achieved using HLA than PLS, and also implies that when the set of spectra has less variability and high signal-to-noise ratio, there is not much room for HLA to improve the prediction.

The improvement made by using HLA over PLS is bigger when there is more fluctuation and noise (multipatient serum experiment) than when the spectra contain

less noise and fluctuation (phosphate buffered saline experiment).

We can also qualitatively compare the results of both HLA and PLS analysis in all three experiments by looking at the prediction plots.

4.6 Time evolution study

We have measured glucose, cholesterol, triglyceride, total protein, and albumin in human blood serum with an uncertainty that is acceptable by clinical standards. In the case of albumin and total protein, the prediction error is almost limited by the reference error, and the predictions could be made with shorter integration times.

A spectral data set of full integration time, 300 seconds was used to calibrate a model. Long integration times make experimental data collection difficult, because a spectrum of a sample may change over a long time due to sample degradations, as mentioned in chapter 3. However, long integration times are preferable for a prediction set, because we need a set of low noise spectra for a high quality model.

On the other hand, short integration times are preferred in clinical applications. In addition to the problem of sample degradation discussed above, long integration times may exceed patients' tolerance.

Figure 4-18 shows how the prediction error changes with integration time in prediction of albumin and total protein concentration. The prediction error drops only slightly although the signal-to-noise ratio increases with the integration time.[2] For albumin, changes in the prediction error are insignificant (Figure 4-18(a)). Even with the increase of the integration time by a factor of 30 from 10 seconds to 300 seconds, the prediction error decreased only by 20%. For total protein, there is no significant change in the prediction error at all (Figure 4-18(b)). Both 10 second data set and 300 second data set have almost the same prediction error, 0.26g/dL.

This study shows that once we have a high quality model, we can drastically reduce integration time for some blood analytes.

[2]The signal-to-noise ratio of a spectrum is proportional to the square root of the integration time.

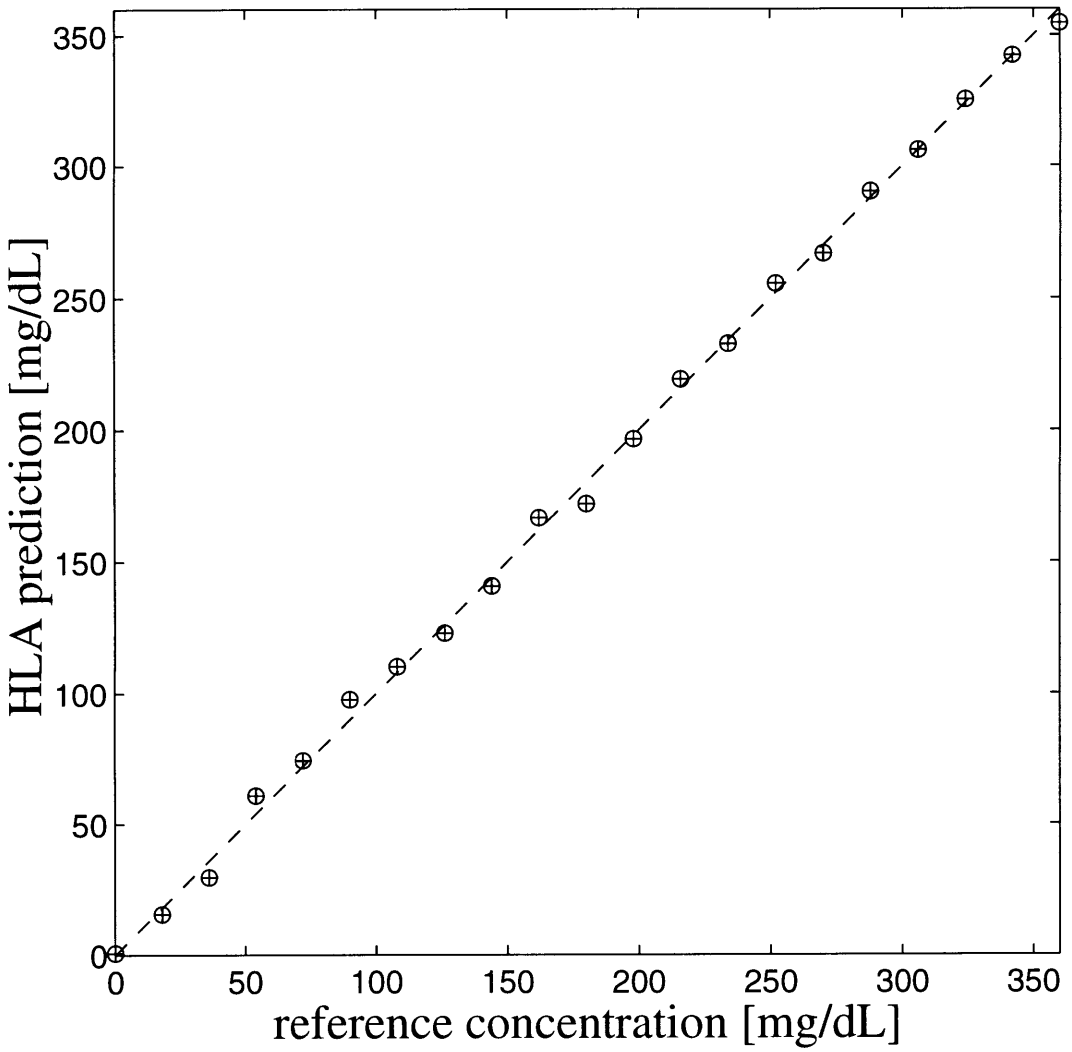

Figure 4-4: HLA prediction plot of glucose concentration in phosphate buffered saline. The dashed line is a 45° line to guide the eye. A prediction plot with zero prediction error has every data point on this line.

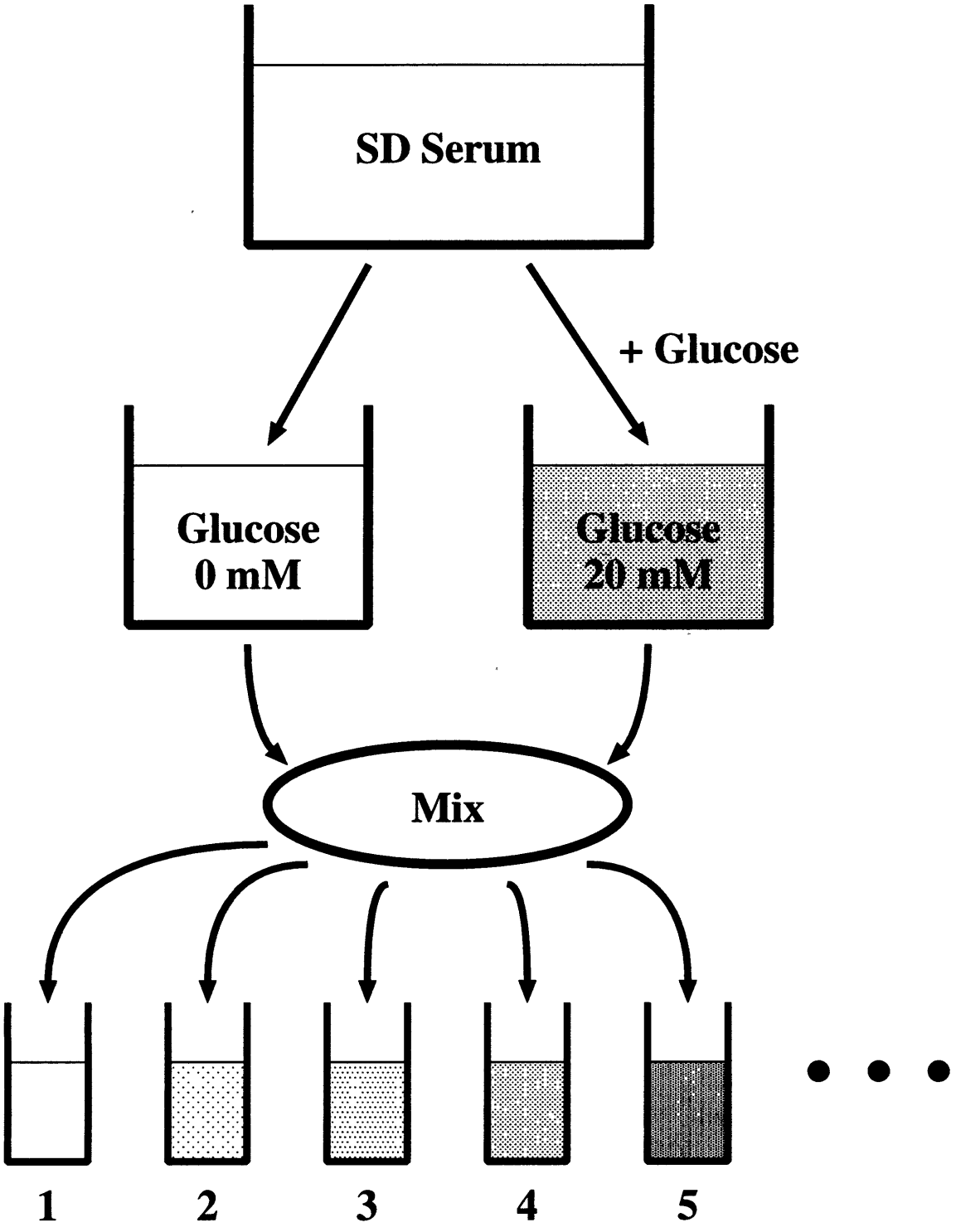

Figure 4-5: Single donor blood serum sample preparation protocol

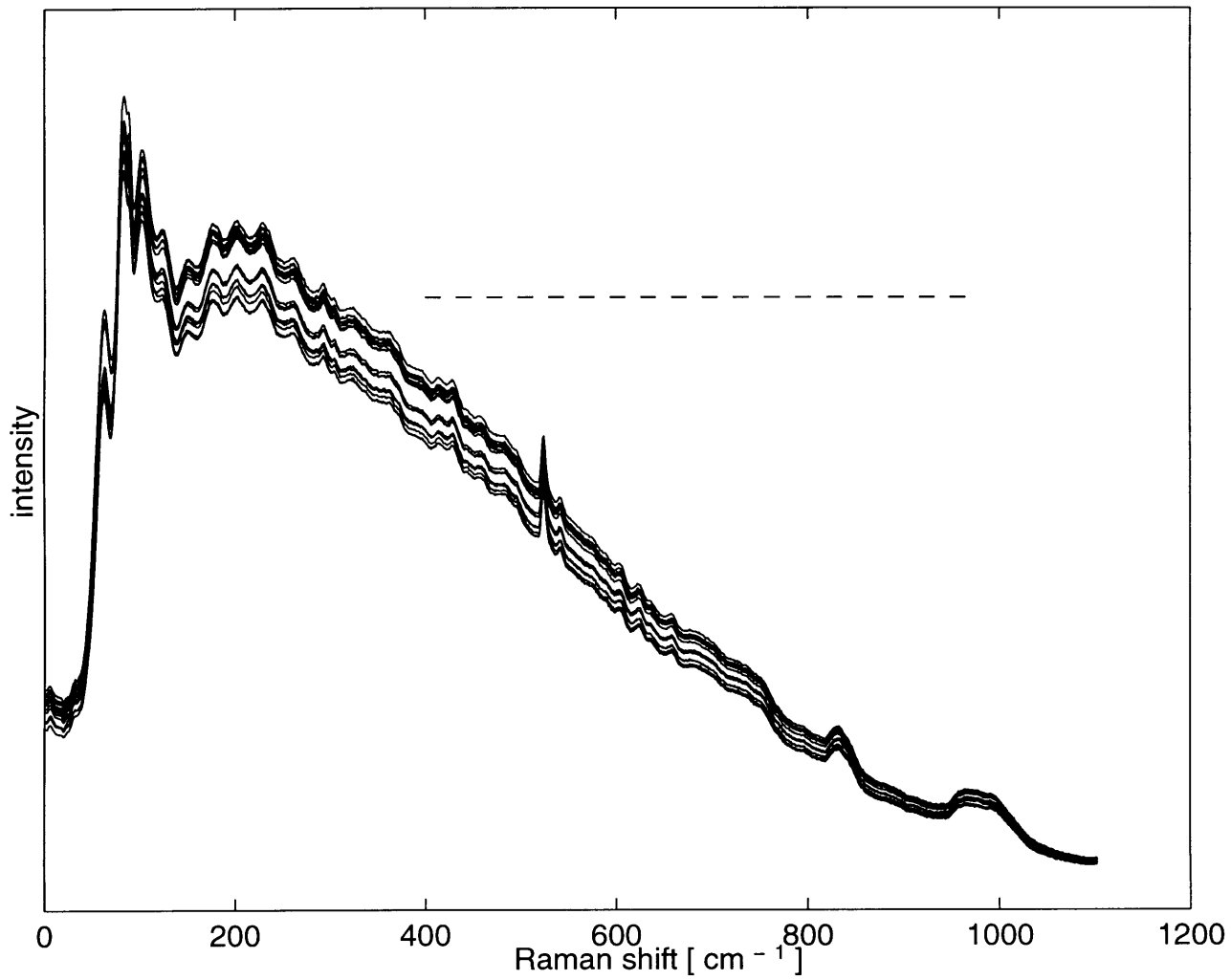

Figure 4-6: Spectra of 16 single-donor human blood serum samples

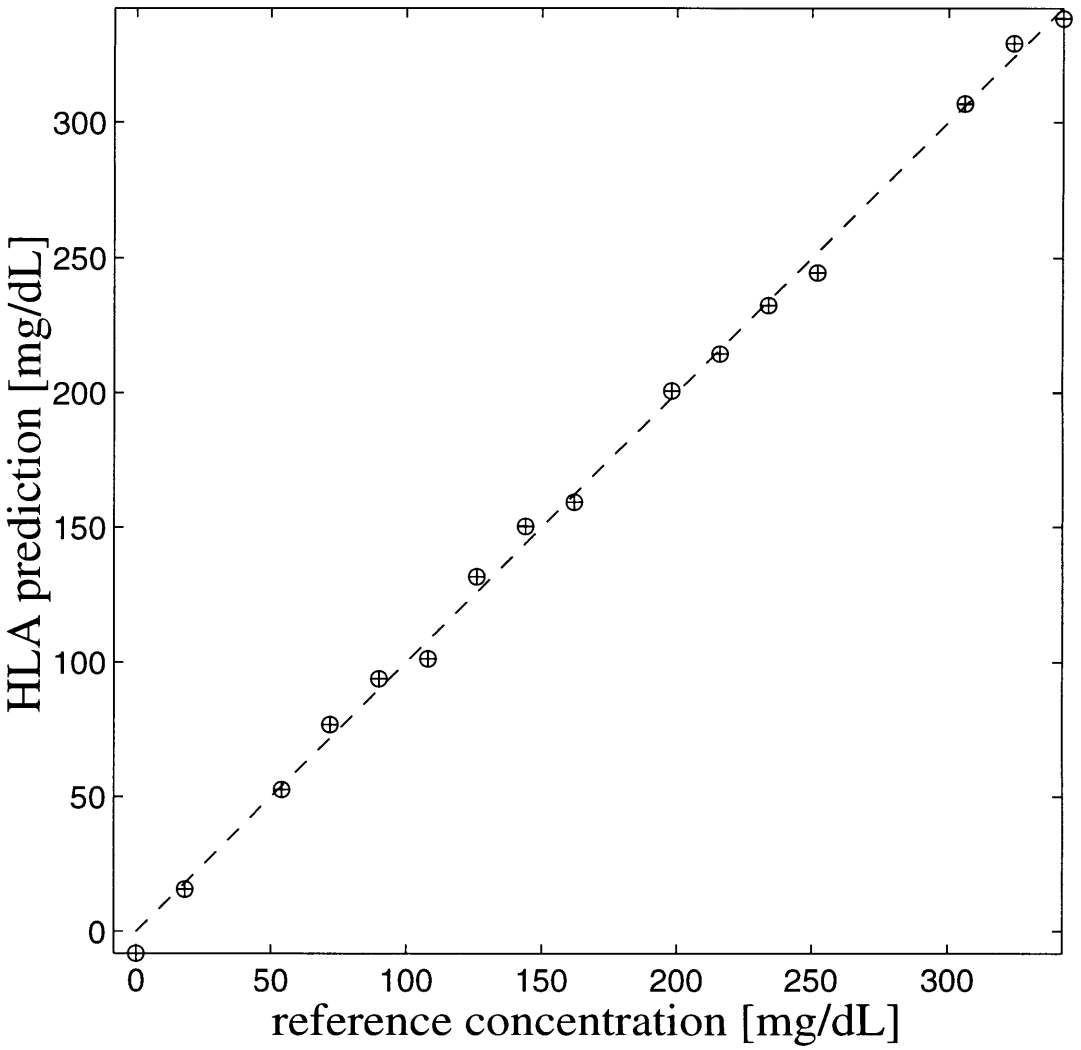

Figure 4-7: HLA prediction plot of glucose concentration in single donor serum.

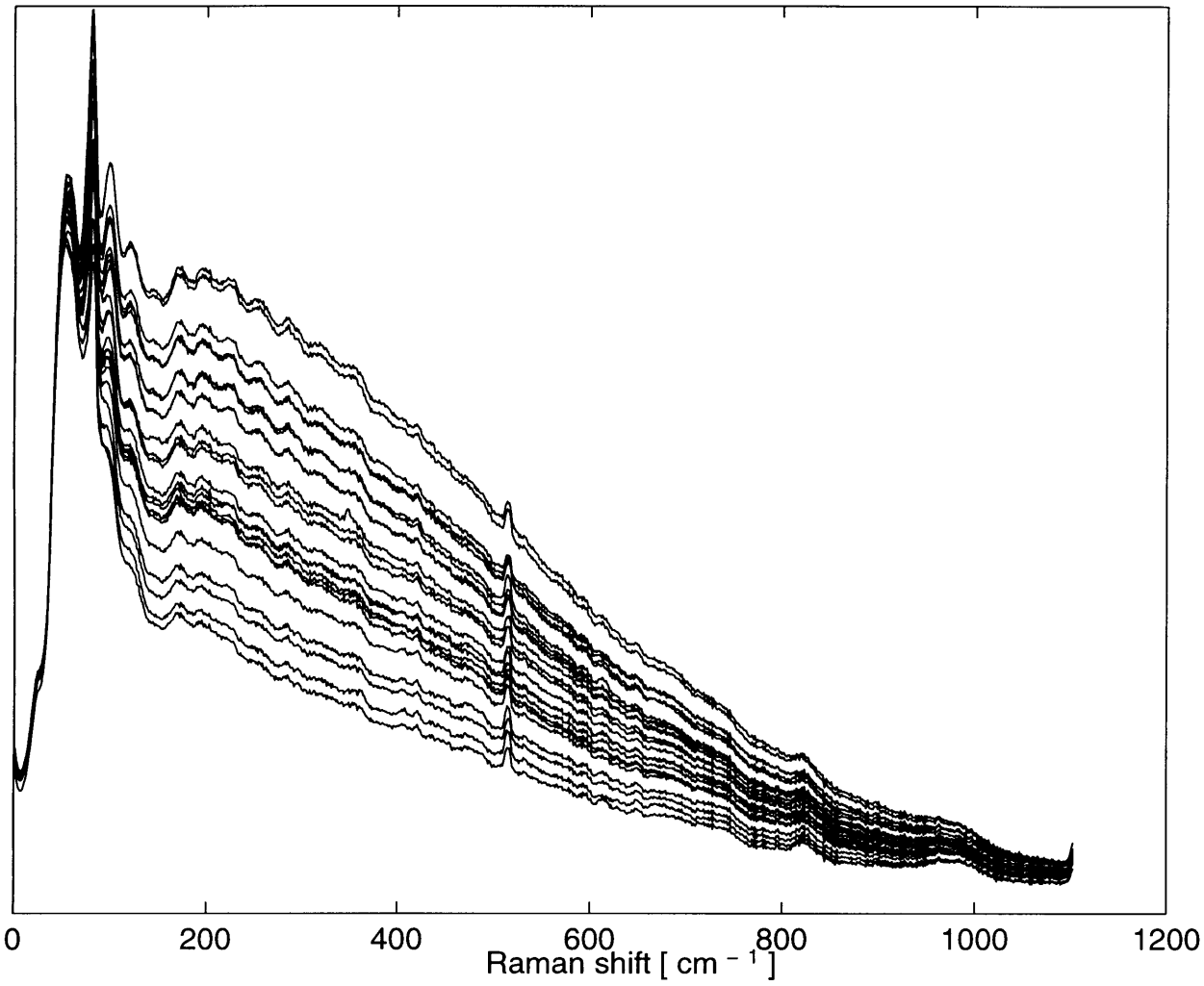

Figure 4-8: Spectra of 24 multi-patient blood serum samples

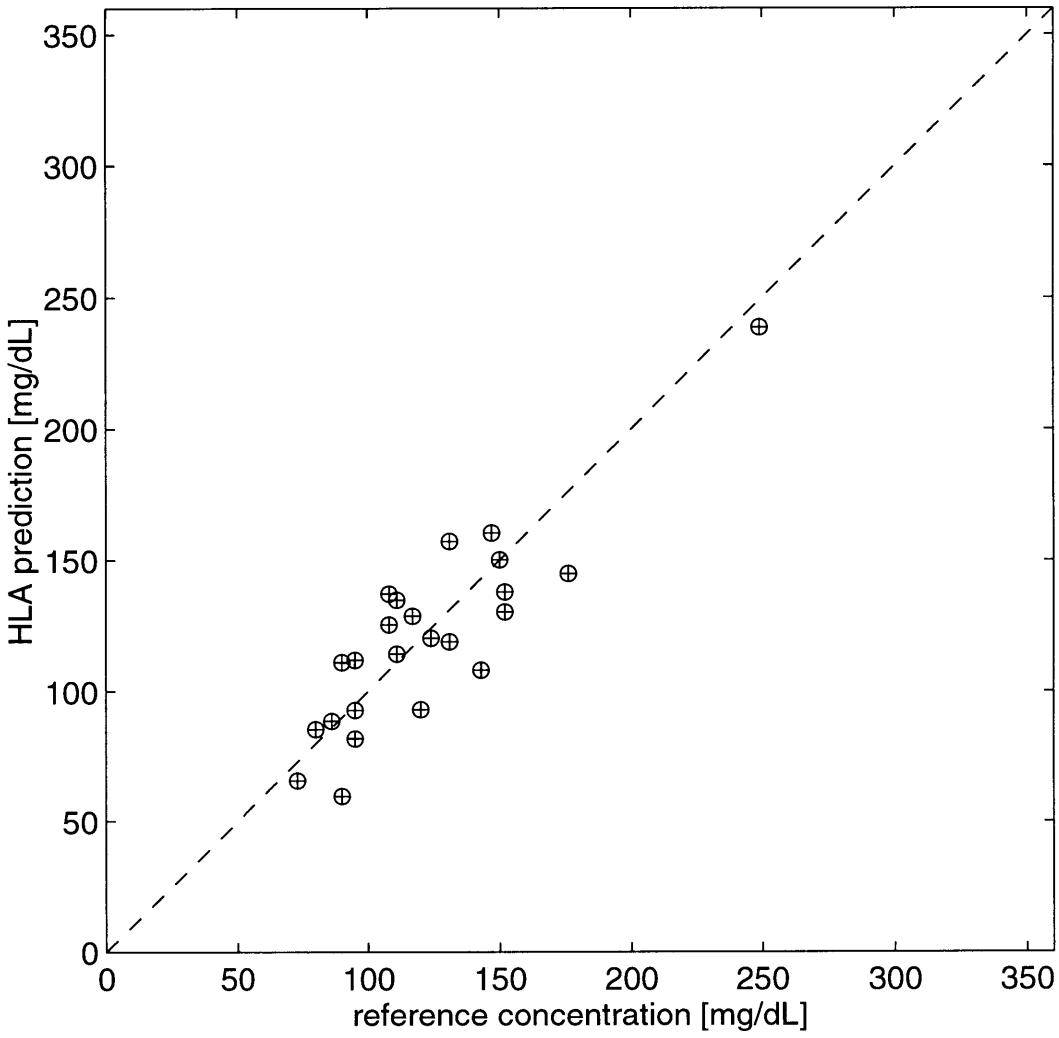

Figure 4-9: HLA prediction plot of glucose concentration in multi-patient serum.

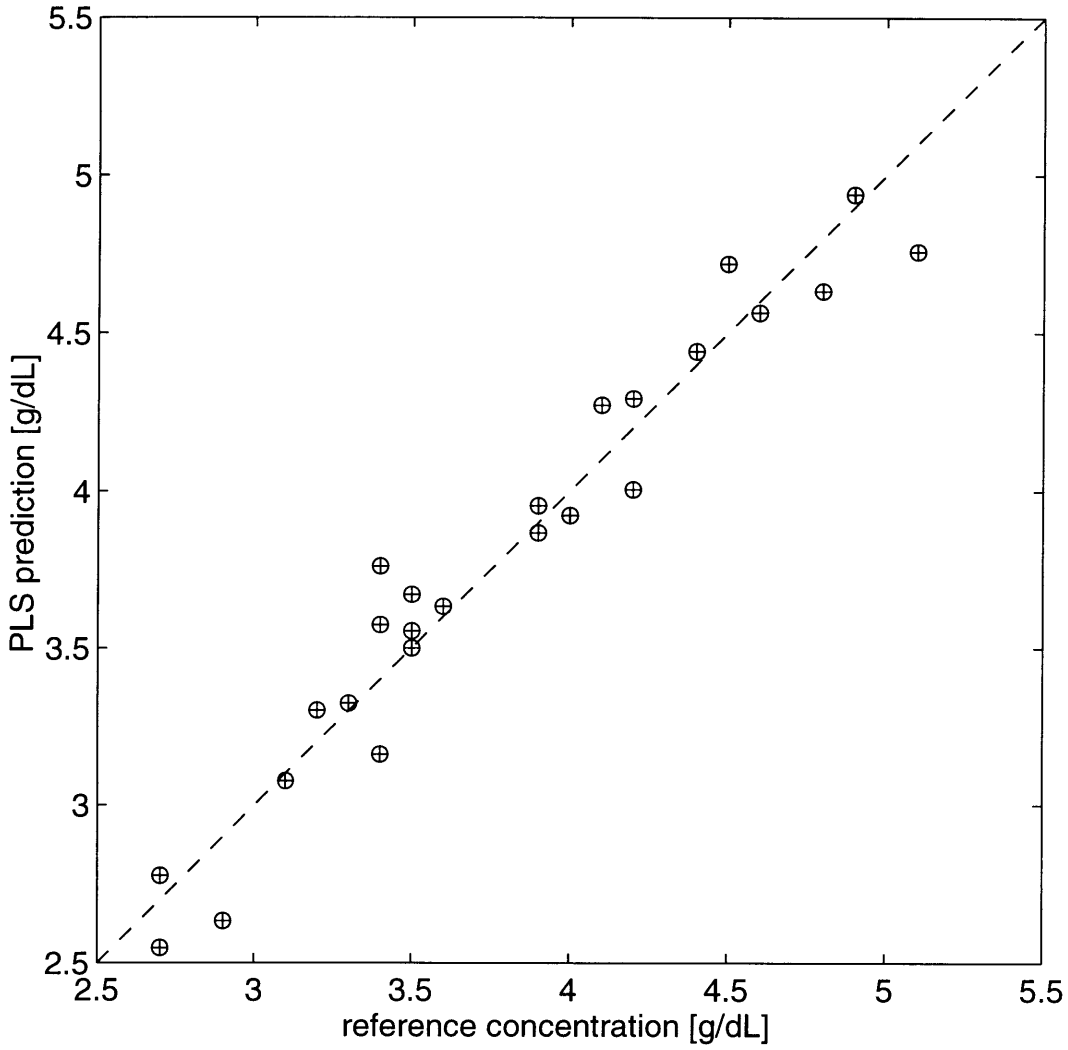

Figure 4-10: PLS prediction plot of albumin concentration in multi-patient serum.

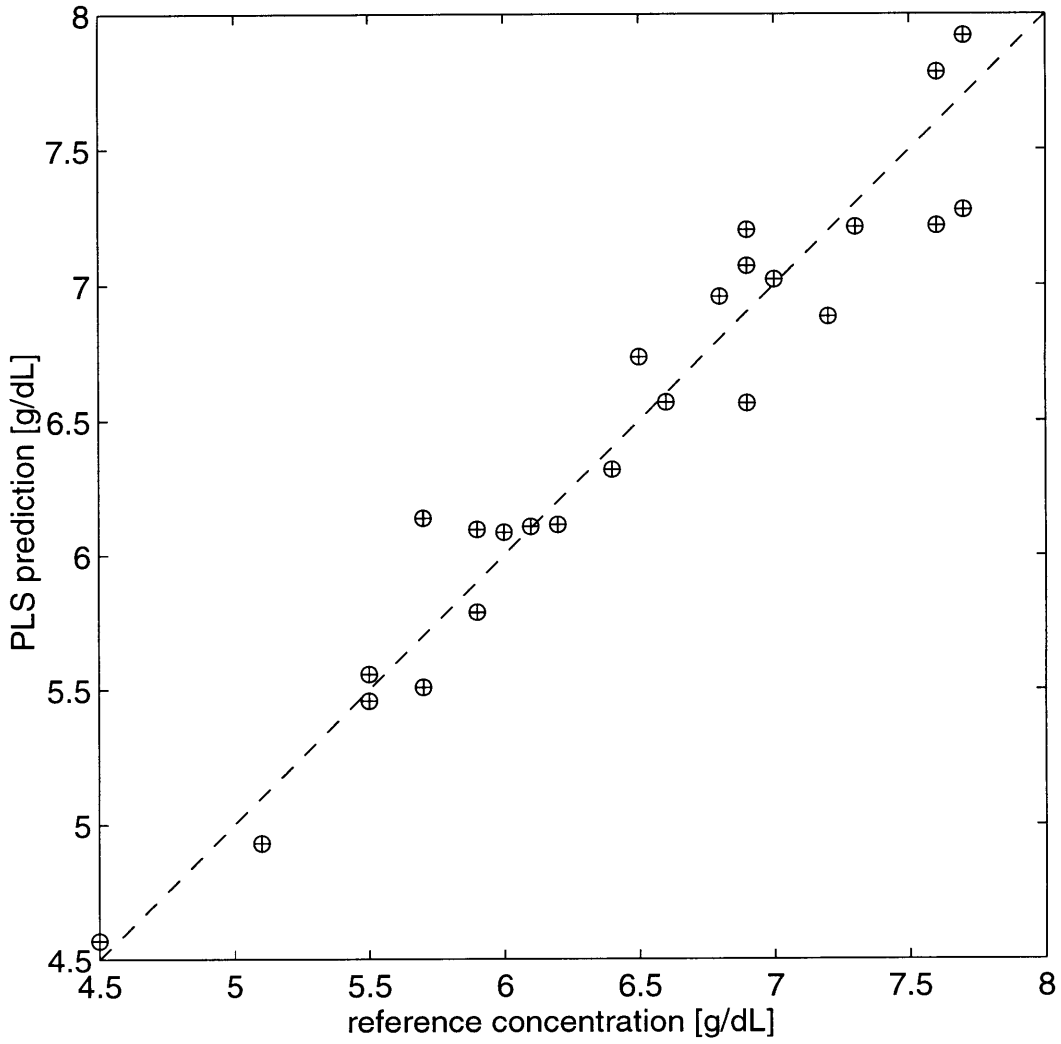

Figure 4-11: PLS prediction plot of total protein concentration in multi-patient serum.

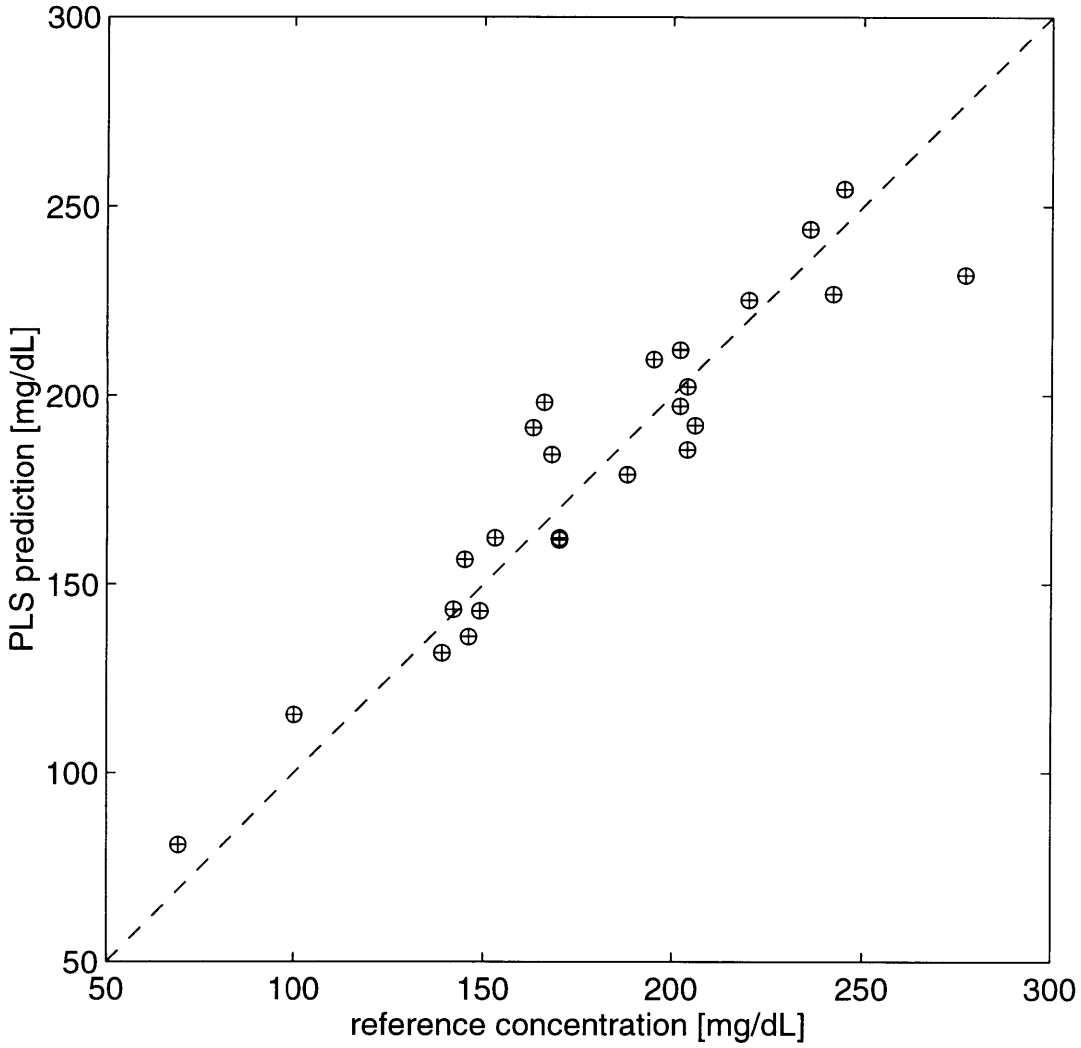

Figure 4-12: PLS prediction plot of cholesterol concentration in multi-patient serum.

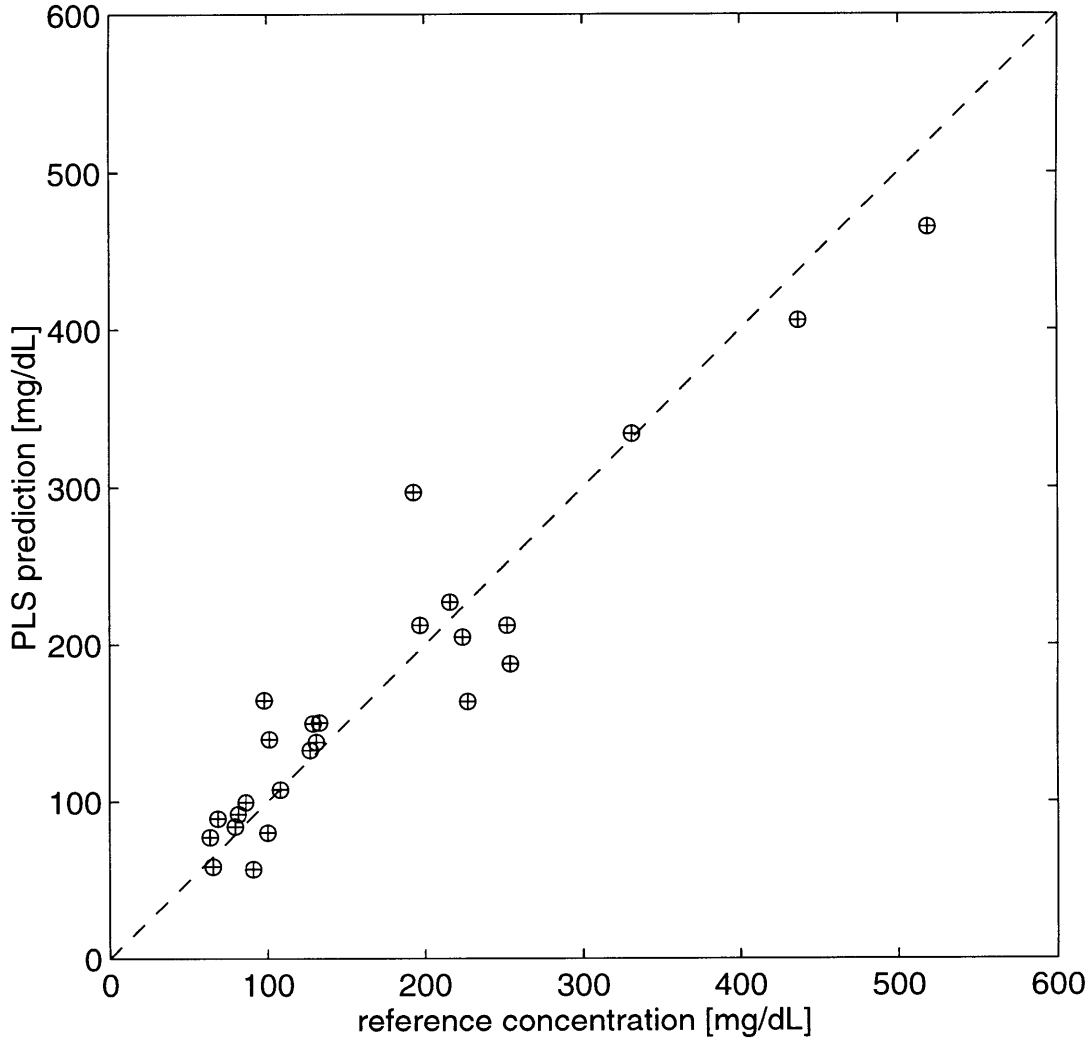

Figure 4-13: PLS prediction plot of triglyceride concentration in multi-patient serum.

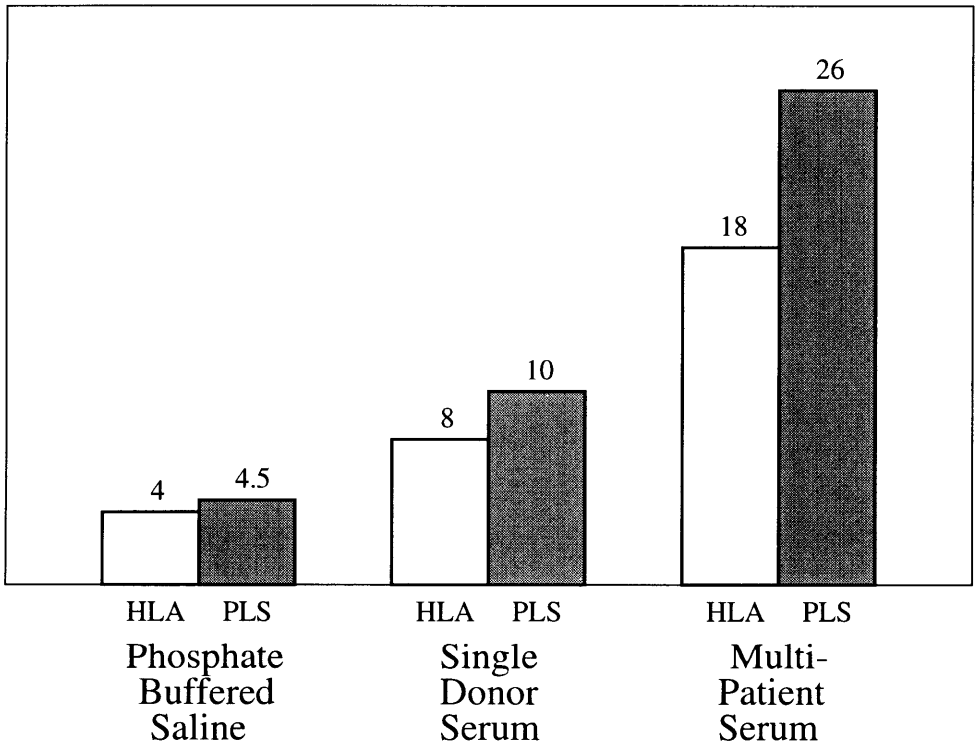

Figure 4-14: Comparison of RMSEP by HLA and PLS in three experiments

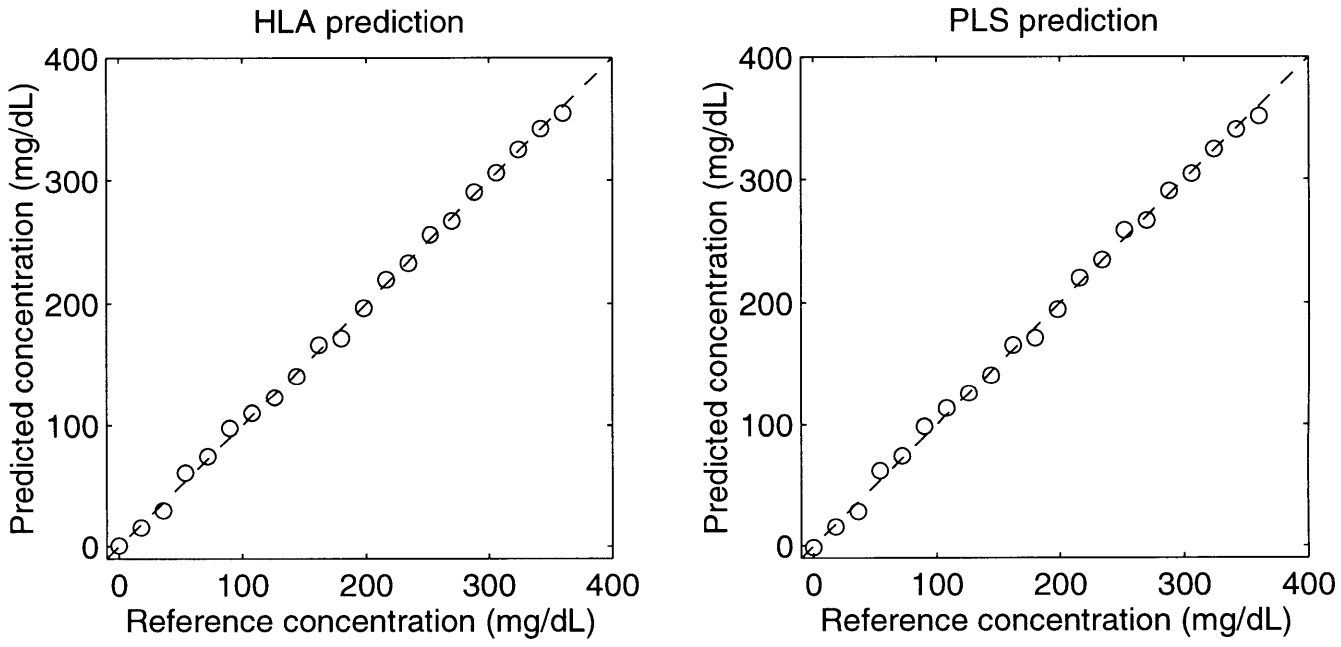

Figure 4-15: Glucose in phosphate buffered saline predicted by HLA and PLS. RMSEP for HLA 4mg/dL; PLS 4.5mg/dL.

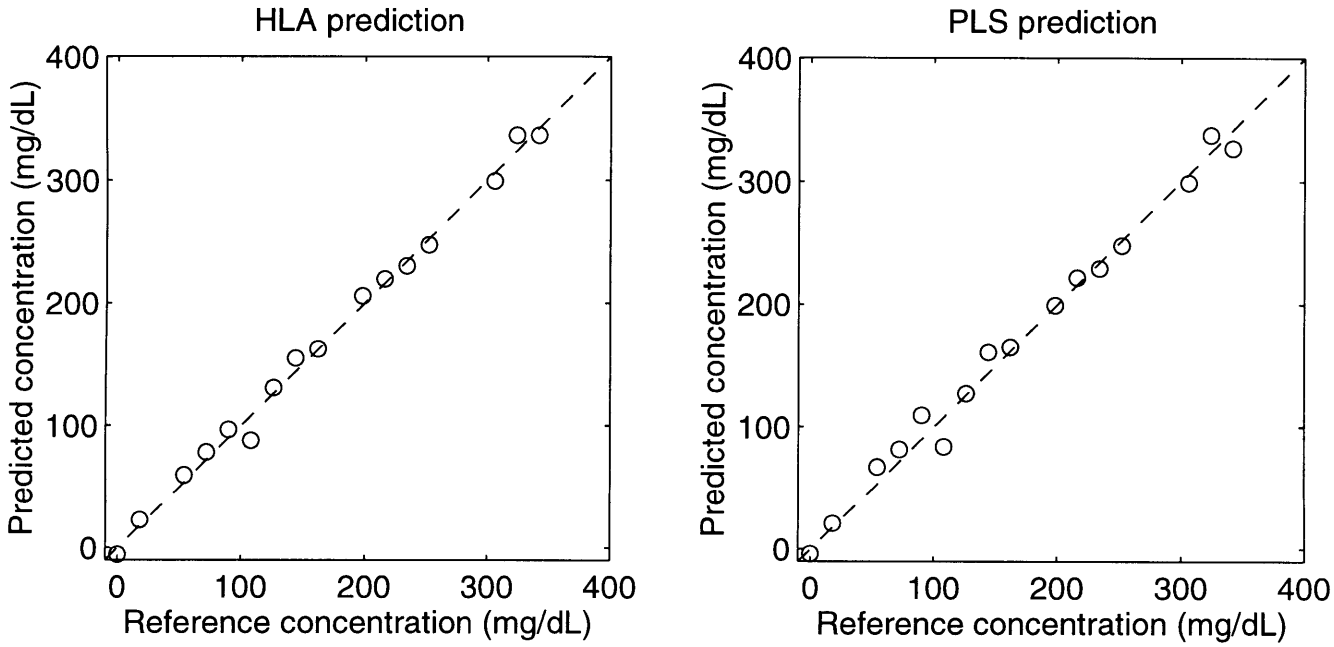

Figure 4-16: Glucose in single donor serum predicted by HLA and PLS. RMSEP for HLA 8mg/dL; PLS 10mg/dL.

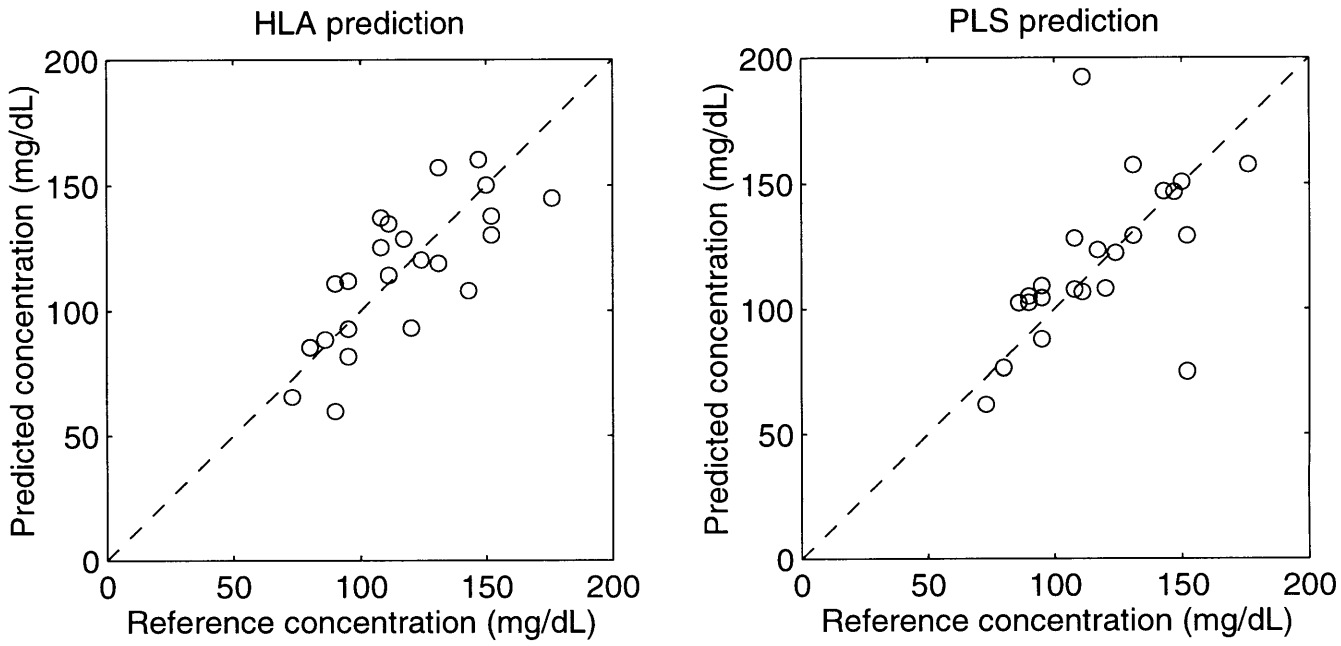

Figure 4-17: Glucose in multi-patient serum predicted by HLA and PLS. RMSEP for HLA 18mg/dL; PLS 26mg/dL.

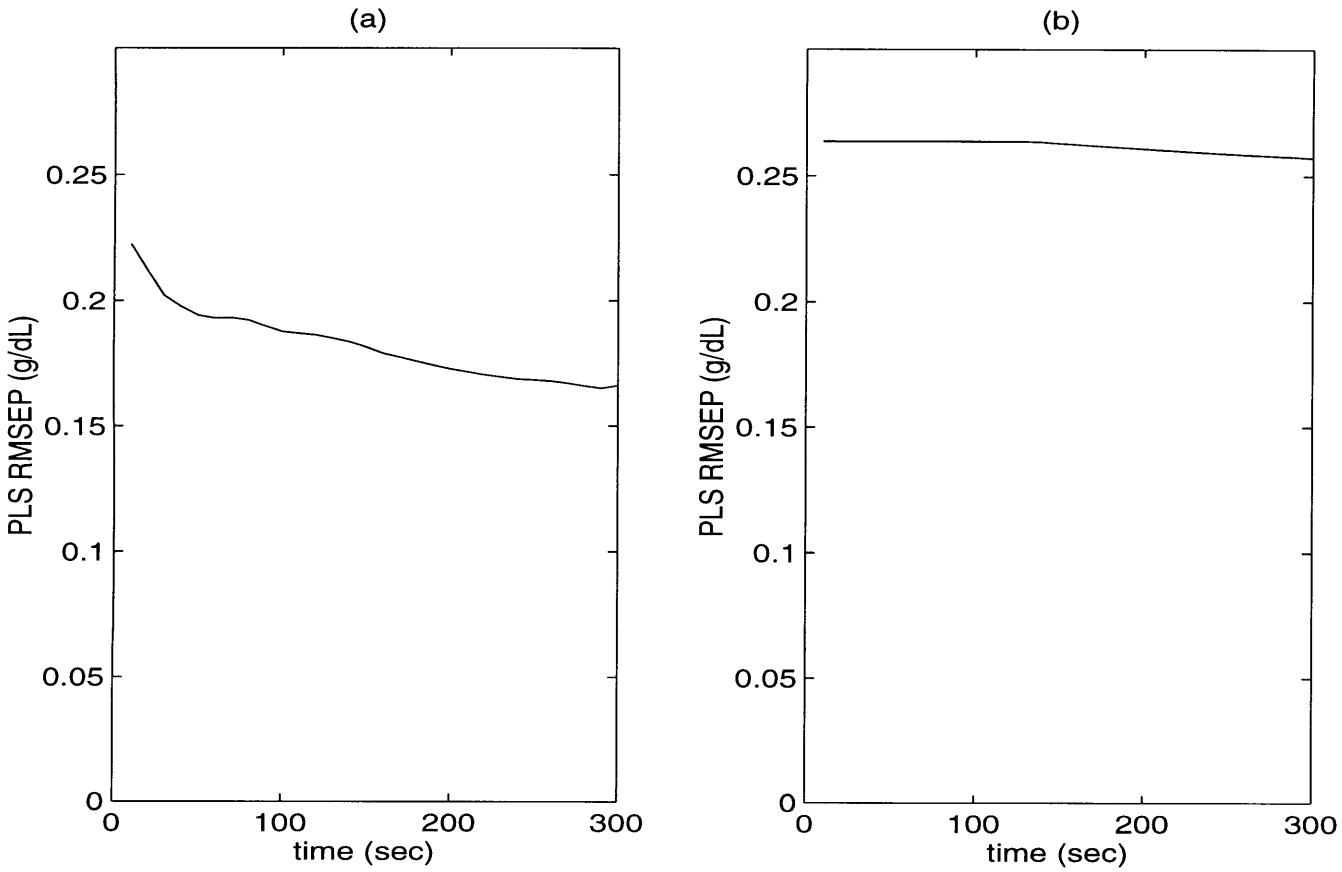

Figure 4-18: Prediction error of (a) albumin and (b) total protein concentration in multipatient blood serum vs spectrum integration time. 300 second data set is used as the calibration set.

Chapter 5

Conclusion and future directions

5.1 Conclusion

A Raman technique to measure blood chemical concentrations in human blood serum was developed. An experimental system was designed. Analysis methods and data processing techniques were studied. A set of experiments was performed.

We measured blood analytes including glucose, albumin, total protein, cholesterol and triglyceride in human blood serum.

5.2 Future directions

5.2.1 Measurement of blood analytes in human whole blood

Human whole blood differs from human serum in that it contains red blood cells and fibrin. By measuring blood analyte concentrations in whole blood directly, one can save time for centrifuging blood samples, because most of the blood analysis in hospital is done with blood serum. We have begun the study of human whole blood.

Human blood serum has relatively low absorption and scattering coefficients, so most of the incident light passes through the blood serum. Human whole blood, as well as other human tissues, has higher scattering coefficients, and the photon migration in human whole blood is very different from that in human blood serum.

The collection optics in our system, which were designed for general Raman spectral measurements, may not be optimal for collecting Raman signal from the whole blood. To optimize the collection optics for a human whole blood experiment, further understanding of the light scattering phenomenon is required.

5.2.2 Indwelling catheter

After measuring blood analytes in human whole blood, this technique can be used with indwelling catheters. By putting an optical probe into a catheter inserted into a vessel, blood analytes can be measured *in vivo*. By reducing the measurement time, continuous measurements are possible, which enables monitoring vital chemical concentrations in operations or bedsides in real-time.

5.2.3 Transcutaneous measurement

One of the great achievements in this research would be the ability to perform transcutaneous measurements.

In a transcutaneous measurement, part of the incident photons come out, and only a small fraction of these photons contain Raman signals from the whole blood. Figure 5-1 shows the photon migration process schematically. This brings into the following problems:

1. Photons may not penetrate deep enough to reach the blood.

2. Signals other than Raman signals from the blood, such as Raman signals from tissue, and fluorescence signals from the blood and tissue co-exist, and have strong intensities.

Transcutaneous measurements require the understanding of four issues including fundamental study of light scattering in blood-tissue matrix, improvements in collection and delivery optics, and improvements in analytical methods.

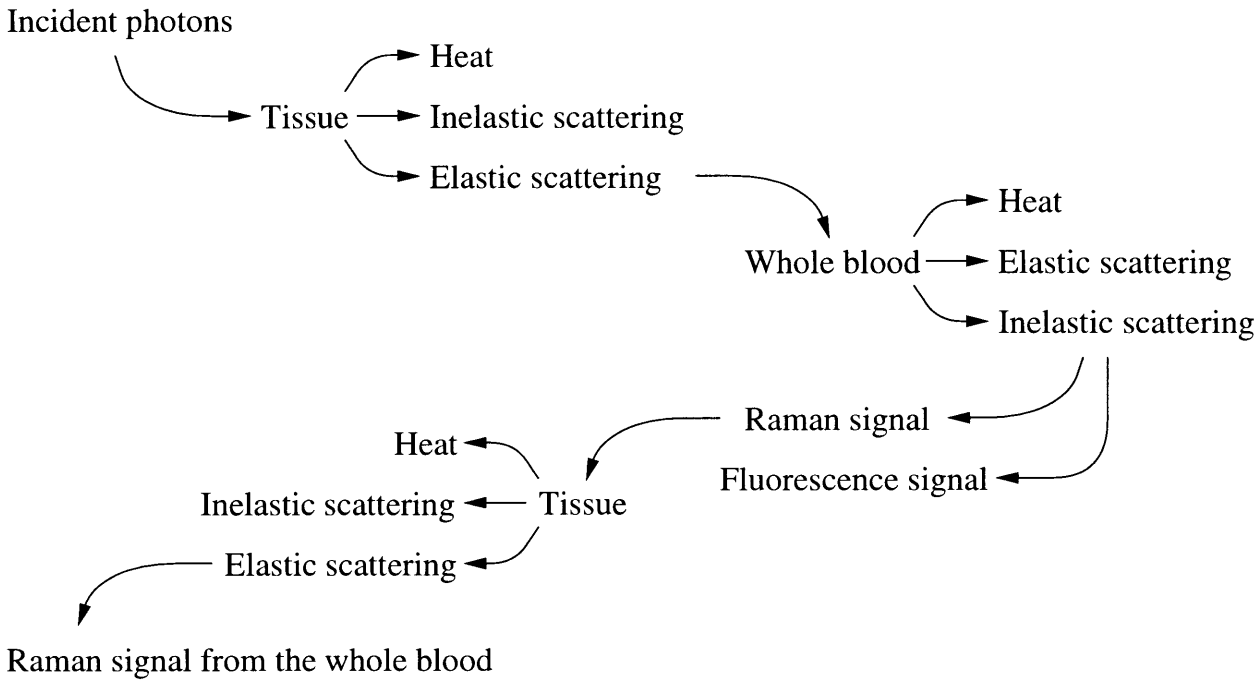

Figure 5-1: Photon migration process in blood-tissue matrix

Fundamental study of light scattering in blood-tissue matrix

As mentioned above, photon migration is more complicated in the human body than in whole blood measurements, in which most of the photons interact only with the whole blood. It is fundamental to understand how light scatters in this complicated medium for designing optimal optics, which are discussed below.

A mathematical model of blood-tissue matrix can be built, and used for the following studies:

- Study of photon migration behavior for different optical parameters, scattering coefficients μ_s' and absorption coefficients μ_a of tissue and blood, and tissue thickness
- Study of photon migration process in inhomogeneous layered media
- Study of the geometric distribution of outcoming Raman signals with different incident beam patterns

Improvements in optics

As shown in Figure 5-1, much of the incident light would be scattered and absorbed in the human body. This results in much weaker Raman signals. Thus, we need to build instruments with higher sensitivity and efficiency. To improve the system the following are required:

- A design for optimized delivery and collection optics is needed to maximize Raman signals from the whole blood. This design can be based on the study of light scattering model mentioned above. Delivery optics should be designed to deliver the light optimally so that most Raman signals from the blood can be generated without damaging tissue. Collection optics should be designed to collect most of Raman signals from the whole blood, and block signals generated by media other than the whole blood. A concept of a confocal microscopic system might be used.

- A different photon detection technique might be used. For example, a Fourier transform spectrometer is known to have higher throughput than a conventional spectrometer.[2] A new detector with higher quantum efficiency in near-infrared wavelengths might be developed soon. Also, a different excitation wavelength can be selected for a possible S/N gain with this new detector.

Bibliography

[1] Joseph John Baraga. *In Situ Chemical Analysis of Biological Tissue: Vibrational Raman Spectroscopy of Human Atherosclerosis.* PhD thesis, Massachusetts Institute of Technology, 1992.

[2] R. J. Bell. *Introductory Fourier Transform Spectroscopy.* Academic Press, New York, 1972.

[3] A. J. Berger and M. S. Feld. Analytical method of estimating chemometric prediction error. *Applied Spectroscopy*, 51(5), 1997.

[4] A. J. Berger, T.-W. Koo, I. Itzkan, and M. S. Feld. An enhanced method of multivariate calibration. *Analytical Chemistry*, January 1998.

[5] B. A. Berkowitz, M. H. Garner, C. A. Wilson, and R. J. T. Corbett. Non-destructive measurement of retinal glucose transport and comsumption in vivo using nmr spectroscopy. *Journal of Neurochemistry*, 64(5), 1995.

[6] Max Diem. *Introduction to Modern Vibrational Spectroscopy.* Wiley-Interscience, New York, 1993.

[7] G.-M. Feng, Y.-C. Huang, J.-G. Chang, M. Chang, and C. Chan. A true phase sensitive optical heterodyne polarimeter on glucose concentration measurement. *Optics Communications*, 41(5-6), 1997.

[8] P. Geladi and B. R. Kowalski. Partial least-squares regression: a tutorial. *Analytica Chimica Acta*, 185, 1986.

[9] D. M. Haaland and E. V. Thomas. Partial least-squares methods for spectral analyses. 1. relatin to other quantitative calibration methods and the extraction of qualitative information. *Analytical Chemistry*, 60, 1988.

[10] A. Lorber and B. R. Kowalski. Estimation of prediction error for multivariate calibration. *Journal of Chemometrics*, 2, 1988.

[11] H. Martens and T. Næs. *Multivariate Calibration.* Wiley, 1989.

[12] Melles Griot. *Melles-Griot Catalogue*, 1995.

[13] K. M. Quan, G. B. Christison, H. A. MacKenzie, and D. Hodgson. Glucose determination by pulsed photoacoustic technique: an experimental study using a gelatin-based tissue phantom. *Physics in Medicine & Biology*, 38(12), 1993.

[14] Schott, Duryea, PA. *Optical Glass.*

[15] A. Sharma and N. Quantrill. Measurement of glucose using fluorescence quenching. *Spectrochimica Acta. Part A: Molecular Spectroscopy*, 50A(6), 1994.

[16] A. E. Siegman. *LASERS.* University Science Books, Mill Valley, CA, 1986.

[17] Warren J. Smith. *Modern Optical Engineering.* McGraw-Hill, New York, 1990.

[18] Spectra Diode Labs, San Jose, CA. *SDL-8630, Tunable Laser Diode, Operator's Manual*, 1994.

[19] R. V. Tarr and P. G. Steffes. *Non-invasive blood glucose measurement system and method using stimulated Raman spectroscopy.* United States Patent 5,243,983, 1990.

[20] M. A. Taylor, M. N. Joones, P. M. Vadgama, and S. P. J. Higson. The characterization of liposomal glucose oxidase electrodes for the measurement of glucose. *Biosensors & Bioelectronics*, 10(3/4), 1995.